JOURNAL OF GEOPHYSICAL RESEARCH, VOL. 113, D07108, doi:10.1029/2007JD009291, 2008

Instability of the axisymmetric monsoon flow and intraseasonal oscillation

Gilles Bellon[1] and Adam H. Sobel[2]

Received 18 August 2007; revised 16 October 2007; accepted 27 December 2007; published 9 April 2008.

[1] A linear model of intermediate complexity based on quasi-equilibrium theory is used in a zonally symmetric aquaplanet configuration to investigate the stability of the mean summer monsoon flow in the south Asian region. In the control case, the mean state has one linearly unstable mode that corresponds in period and structure to the variability in the nonlinear model described by Bellon and Sobel (2008) and to the observed 30- to 60-d mode of intraseasonal variability. This mode features propagation of the precipitation anomalies from the equator to the monsoon trough around 20°N. Both the period of this mode and its direction of propagation are determined by the direction and magnitude of the mean meridional baroclinic flow. The wind-induced surface heat fluxes associated with the surface westerlies in the northern tropics are an important contributor to the instability of the mode. The mechanisms of propagation and reinitiation of convection are further described. (1) Meridional advection of vorticity by the mean flow is responsible for the creation of free-tropospheric vorticity north of the convection center. This vorticity in turn creates boundary layer convergence via Coriolis acceleration and subsequent northward movement of the convection. (2) Meridional advection of zonal momentum creates equatorial free-tropospheric easterlies on the equator. These easterlies in turn generate low-level convergence via the β term of the Coriolis acceleration and cause the reemergence of convection at the equator.

Citation: Bellon, G., and A. H. Sobel (2008), Instability of the axisymmetric monsoon flow and intraseasonal oscillation, *J. Geophys. Res.*, *113*, D07108, doi:10.1029/2007JD009291.

1. Introduction

[2] The monsoons are characterized by strong intraseasonal variability that causes alternating rainy and dry periods, the ''active phases'' and ''breaks'' of the monsoon. In the south Asian region, the intraseasonal variability can be seen as a seesaw between two longitudinal bands of maximum precipitation: the equatorial Tropical Convergence Zone (TCZ) and the monsoonal TCZ around 20°N [*Sikka and Gadgil*, 1980; *Goswami and Ajaya Mohan*, 2001]. Spectra of the variability show two significant peaks in the intraseasonal range: one at 10–20 d and one at 30–60 d [*Goswami*, 2005]. The 10- to 20-d mode seems to be associated with disturbances propagating from the Pacific warm pool to south Asia that appear as Rossby waves deviated poleward by the mean monsoon flow [*Chatterjee and Goswami*, 2004; *Wang and Xie*, 1997]. On the other hand, the 30- to 60-d mode is associated with northward propagation of the TCZ from its preferred equatorial position to its preferred monsoon location around 20°N.

[3] Composites of the 30- to 60-d mode show its characteristic dynamical structure. Convergence in the Atmospheric Boundary Layer (ABL) leads the convection by a few degrees [*Kemball-Cook and Wang*, 2001; *Lawrence and Webster*, 2002; *Jiang et al.*, 2004; *Goswami*, 2005]. Positive relative vorticity in the free troposphere is almost colocated with, or slightly leads the ABL convergence [*Jiang et al.*, 2004; *Goswami*, 2005]. The reinitiation of convection at the equator is also preceded by ABL convergence there [*Wang et al.*, 2006].

[4] Different mechanisms have been proposed to explain the northward propagation of the TCZ. *Goswami and Shukla* [1984] showed using an axisymmetric GCM that the interaction between convection and dynamics can cause an intraseasonal oscillation in the 30- to 60-d range characterized by northward propagation of the precipitation anomaly. This idea has been explored in subsequent studies using simple models. The seasonal northward gradient of moist static stability has been proposed as the crucial element causing the northward propagation [*Gadgil and Srinivasan*, 1990; *Nanjundiah et al.*, 1992].

[5] A recent theoretical analysis proposed two mechanisms for the northward propagation [*Jiang et al.*, 2004]: a ''moisture-convection feedback mechanism'' that explains the northward propagation near the equator by the anomalous advection of the mean humidity and a ''vertical shear mechanism'' that explains the off-equatorial propagation and the mode's dynamical structure. The vertical shear

[1]Department of Applied Physics and Applied Mathematics, Columbia University, New York, New York, USA.
[2]Department of Applied Physics and Applied Mathematics and Department of Earth and Environmental Sciences, Columbia University, New York, New York, USA.

0148-0227/08/2007JD009291$09.00

mechanism involves the creation of barotropic vorticity north of the center of convection by anomalous vertical advection of the mean easterly vertical shear. This mechanism was shown to be important in a simple, quasi-linear model [*Drbohlav and Wang*, 2005].

[6] In a recent study [*Bellon and Sobel*, 2008, hereinafter referred to as BS] we presented simulations of the 30- to 60-d oscillation in an intermediate-complexity axisymmetric model from the Quasi-equilibrium Tropical Circulation Model (QTCM) family [*Neelin and Zeng*, 2000; *Zeng et al.*, 2000]. This model in an aquaplanet configuration simulates the qualitative features of the seasonal monsoon mean convincingly. This model also simulates convincingly the structure of the 30- to 60-d mode, with the maxima of ABL convergence and barotropic vorticity leading the maximum of precipitation. We studied the bifurcation tree of the nonlinear system and showed the crucial role of the wind-induced surface heat fluxes [*Emanuel*, 1987; *Neelin et al.*, 1987] for the development of the intraseasonal oscillation in the model. We showed that the inclusion of a dynamic and thermodynamic boundary layer in the model were necessary to the existence of the oscillation, but did not analyze the mechanism of the northward propagation.

[7] In BS, we showed that the instability in our model was essentially linear. In the present work, we use the linearized model to study the fundamentals of the instability, the scale selection, the northward propagation, and the structure of the precipitation patterns. Section 2 describes the model in its linear version and its basic results and section 3 investigates the role of the different components of the mean seasonal state. A further stripped-down model is introduced in section 4 to further understand the oscillation and clarify its mechanisms (section 5). The sensitivity of the oscillation to the main parameters of the model is described in Appendix A.

2. Linear Model

[8] In this study, we use the linear version of the model used in BS, which is the prototype QTCM2 in an equatorial β-plane axisymmetric configuration. The QTCM family of models is based on the Galerkin projection of the primitive equations on a limited number of reference vertical profiles derived from asymptotic solutions of quasi-equilibrium theory [*Neelin and Zeng*, 2000; *Zeng et al.*, 2000]. In the QTCM2, the vertical structure of the wind has three degrees of freedom: one barotropic mode and one baroclinic mode in the free troposphere, and a mode for the Atmospheric Boundary Layer (ABL) flow represented by a slab of constant depth in which the wind is uniform with height. The thermodynamic variables (temperature and humidity) each have two degrees of freedom: one for the free troposphere and one for the well-mixed ABL. An exhaustive description of the model is given by BS and by *Sobel and Neelin* [2006]. Here, we summarize the linearized version of the model.

2.1. Summary of the Vertical Structure

[9] Each variable x in the axisymmetric primitive equations (horizontal velocity $\mathbf{v}(y, p, t)$, vertical speed $\omega(y, p, t)$, temperature $T(y, p, t)$, and humidity $q(y, p, t)$) is described by its deviation from a reference profile X_r projected on a few perturbation profiles X_i:

$$x(y,p,t) = X_r(p) + \sum_{i\in\{0,1,b\}} X_i(p)x_i(y,t), \tag{1}$$

where y the latitude, p the pressure, and t the time. The perturbation profiles of temperature (respectively humidity, horizontal and vertical velocities) are noted a_i (resp. b_i, V_i and Ω_i). The subscript 0 indicates the barotropic mode, 1 the baroclinic mode and a subscript b [not to be confused with the moisture profiles $b_i(p)$] indicates the ABL mode. The perturbation functions and their relations with each other are described in detail in BS. In particular, (1) $V_r = 0$; (2) $a_0 = 0$ and $b_0 = 0$; (3) $V_0(p) = 1$; (4) $V_1(p) = a_1^+ - \langle a_1^+ \rangle$, with $a_1^+ = \int_p^{p_e} a_1\, d\ln\dot{p}$; and (5) $\Omega_i(p) = \int_{p_t}^{p} V_i d\dot{p}$, where $\langle\ \rangle$ indicates the free-tropospheric average, p_e is the pressure at the top of the ABL, and p_t the pressure at the tropopause. $\kappa a_1^+(p)$ is the perturbation of geopotential $\phi(p)$ associated to the perturbation of temperature $a_1(\dot{p})$ for $p < \dot{p} < p_e$, with $\kappa = R/C_p$ the ratio of the gas constant for air R by the heat capacity of air at constant pressure C_p.

[10] We can rewrite (1) in terms of the sum of a time mean and perturbations:

$$x(y,p,t) = \bar{x}(y,p) + \sum_{i\epsilon\{0,1,b\}} X_i(p)x_i'(y,t) \tag{2}$$

where the overbar indicates the time mean and the prime indicate the perturbation from this mean. We have:

$$\bar{x}(y,p) = X_r(p) + \sum_{i\epsilon\{0,1,b\}} X_i(p)\bar{x}_i(y) \tag{3}$$

2.2. Linear Equations

[11] The properties of the vertical structure are used to project the primitive equations and obtain the time evolution of the perturbation x_i'. Note that the temperatures and humidities are expressed in energy units, i.e., temperature in Kelvin multiplied by the heat capacity of air at constant pressure C_p and specific humidity in *kg*/*kg* multiplied by the latent heat of vaporization L_v.

[12] The linearized free-tropospheric temperature and moisture equations are:

$$\begin{aligned}\langle a_1\rangle\left[\partial_t T_1' + \overline{\mathbf{v}}_0\cdot\nabla T_1' + \mathbf{v}_0'\cdot\nabla\overline{T}_1\right] &+ \left(\langle s\rangle' - s^{\dagger\prime}\right)(\nabla\cdot\overline{\mathbf{v}}_0)\\ &+ \left(\langle\overline{s}\rangle - \overline{s}^{\dagger}\right)\left(\nabla\cdot\mathbf{v}_0'\right) + \langle a_1 V_1\rangle\left(\overline{\mathbf{v}}_1\cdot\nabla T_1' + \mathbf{v}_1'\cdot\nabla\overline{T}_1\right)\\ &+ M_{sp1}T_1'(\nabla\cdot\overline{\mathbf{v}}_1) + \overline{M}_{s1}\left(\nabla\cdot\mathbf{v}_1'\right)\\ &= \langle Q_c'\rangle + \langle Q_R'\rangle + \langle a_1\rangle k_q\nabla^2 T_1',\end{aligned} \tag{4}$$

where $s = T + \phi$ is the dry static energy, and

$$\begin{aligned}\langle b_1\rangle\left[\partial_t q_1' + \overline{\mathbf{v}}_0\cdot\nabla q_1' + \mathbf{v}_0'\cdot\nabla\overline{q}_1\right] &+ \left(\langle q\rangle' - q^{\dagger\prime}\right)(\nabla\cdot\overline{\mathbf{v}}_0)\\ &+ \left(\langle\overline{q}\rangle - \overline{q}^{\dagger}\right)\left(\nabla\cdot\mathbf{v}_0'\right) + \langle b_1 V_1\rangle\left(\overline{\mathbf{v}}_1\cdot\nabla q_1' + \mathbf{v}_1'\cdot\nabla\overline{q}_1\right)\\ &- M_{qp1}q_1'(\nabla\cdot\overline{\mathbf{v}}_1) - \overline{M}_{q1}\left(\nabla\cdot\mathbf{v}_1'\right)\\ &= \langle Q_q'\rangle + \langle b_1\rangle k_q\nabla^2 q_1'.\end{aligned} \tag{5}$$

$\nabla = (0, \partial_y)$ in the axisymmetric framework used here, and we used the projected continuity equation $\omega_i = -\nabla\cdot\mathbf{v}_i$ to replace the vertical speeds by the divergences. The super-

script dagger (†) indicates the value advected by the vertical motion at the ABL top. We use a centered formulation as proposed in [*Sobel and Neelin*, 2006]:

$$x^{\dagger} = \frac{1}{2}(x_b + x_e), \tag{6}$$

with $x = s$, q, or $\mathbf{v}$. The subscript e indicates the value just above ABL top. The nonlinear model in BS used an upwind formulation, but that formulation cannot be simply linearized. Changing from the upwind to the centered scheme causes only small differences in the nonlinear simulations (not shown).

[13] Q_c, Q_q, and Q_R are respectively the convective heating, convective moistening and radiative heating, and k_q is the horizontal diffusivity coefficient for humidity and temperature. The free-tropospheric average of the mean energy and humidity include the reference profiles: $\langle \overline{s} \rangle = \langle s_r \rangle + \langle a_1 + \kappa a_1^+ \rangle \overline{T}_1$ and $\langle \overline{q} \rangle = \langle q_r \rangle + \langle b_1 \rangle \overline{q}_1$. We also have: $\langle s \rangle' = \langle a_1 + \kappa a_1^+ \rangle T_1'$ and $\langle q \rangle' = \langle b_1 \rangle q_1'$. We have further defined the gross dry static stabilities and gross moisture stratifications for each mode:

$$\begin{aligned} M_{si} &= \overline{M}_{si} + M_{spi} T_1' \quad \text{with } \overline{M}_{si} = M_{sri} + M_{spi}\overline{T}_1, \\ M_{qi} &= \overline{M}_{qi} + M_{qpi} q_1' \quad \text{with } \overline{M}_{qi} = M_{qri} + M_{qpi}\overline{q}_1, \end{aligned} \tag{7}$$

where the index i can be either 0 or 1. The coefficients M_{sri} and M_{spi} (respectively M_{qri} and M_{qpi}) result from the integration of the vertical profiles of wind and dry static energy (resp. humidity):

$$M_{sri} = -\langle \Omega_i \partial_p s_r \rangle \quad \text{and} \quad M_{spi} = -\langle \Omega_i \partial_p (a_1 + \kappa a_1^+) \rangle,$$

$$M_{qri} = \langle \Omega_i \partial_p q_r \rangle \quad \text{and} \quad M_{qpi} = \langle \Omega_i \partial_p b_1 \rangle,$$

where $s_r = T_r + \kappa \int_p^{p_s} T_r \, d\ln \grave{p}$ is the reference dry static energy profile, with p_s the surface pressure.

[14] The linearized equations for barotropic and baroclinic velocities are

$$\begin{aligned} &\partial_t \mathbf{v}_0' + \nabla \cdot (\overline{\mathbf{v}}_0 \mathbf{v}_0' + \mathbf{v}_0' \overline{\mathbf{v}}_0) + \langle V_1^2 \rangle \nabla \cdot (\overline{\mathbf{v}}_1 \mathbf{v}_1' + \mathbf{v}_1' \overline{\mathbf{v}}_1) \\ &\quad - \mathbf{v}^{\dagger\prime} (\nabla \cdot \overline{\mathbf{v}}_0) - \overline{\mathbf{v}}^{\dagger} (\nabla \cdot \mathbf{v}_0') + f \hat{\mathbf{k}} \times \mathbf{v}_0' \\ &\quad = -\nabla \left(\kappa a_b^{+e} s_b' + \kappa \langle a_1^+ \rangle T_1' + \phi_s' \right) + k_v \nabla^2 \mathbf{v}_0', \end{aligned} \tag{8}$$

and

$$\begin{aligned} &\partial_t \mathbf{v}_1' + (\overline{\mathbf{v}}_0 \cdot \nabla) \mathbf{v}_1' + (\mathbf{v}_0' \cdot \nabla) \overline{\mathbf{v}}_1 + (\overline{\mathbf{v}}_1 \cdot \nabla) \mathbf{v}_0' + (\mathbf{v}_1' \cdot \nabla) \overline{\mathbf{v}}_0 \\ &\quad + \frac{\langle V_1^3 \rangle}{\langle V_1^2 \rangle} (\overline{\mathbf{v}}_1 \cdot \nabla \mathbf{v}_1' + \mathbf{v}_1' \cdot \nabla \overline{\mathbf{v}}_1) \\ &\quad + \frac{\langle V_1^3 \rangle}{2 \langle V_1^2 \rangle} \cdot \left[\mathbf{v}_1' (\nabla \cdot \overline{\mathbf{v}}_1) + \overline{\mathbf{v}}_1 (\nabla \cdot \mathbf{v}_1') \right] \\ &\quad - \frac{1}{2} \left[\frac{V_{1e}^2}{\langle V_1^2 \rangle} - 1 \right] \cdot \left[\mathbf{v}_1' (\nabla \cdot \overline{\mathbf{v}}_0) + \overline{\mathbf{v}}_1 (\nabla \cdot \mathbf{v}_0') \right] \\ &\quad - \frac{V_{1e}}{\langle V_1^2 \rangle} \cdot \left[\left(\mathbf{v}^{\dagger\prime} - \mathbf{v}_e' \right) (\nabla \cdot \overline{\mathbf{v}}_0) + \left(\overline{\mathbf{v}}^{\dagger} - \overline{\mathbf{v}}_e \right) (\nabla \cdot \mathbf{v}_0') \right] \\ &\quad + f \hat{\mathbf{k}} \times \mathbf{v}_1' \\ &\quad = -\kappa \nabla T_1' - \epsilon_1 \mathbf{v}_1' + k_v \nabla^2 \mathbf{v}_1', \end{aligned} \tag{9}$$

where $f = \beta y$ is the Coriolis parameter, $\hat{\mathbf{k}}$ the vertical unit vector, ϕ_s' is the surface geopotential, k_v is the horizontal diffusivity coefficient for momentum, and ϵ_1 is a coefficient that accounts for vertical mixing by small eddies. $\mathbf{v}_e = \mathbf{v}_0 + V_{1e}\,\mathbf{v}_1$, where we use the notational shorthand $V_{1e} \equiv V_1(p_e)$. The coefficient a_b^{+e} comes from integrating temperature to obtain geopotential using hydrostatic balance, and is defined by:

$$a_b^{+e} = \int_{p_e}^{p_s} a_b \, d\ln p = a_b^+(p_e). \tag{10}$$

[15] For the boundary layer, the procedure is essentially the same, but simpler, as each variable has only one mode, and each prognostic variable q, s, $\mathbf{v}$ is assumed uniform in the vertical. We thus have the following equations for ABL dry static energy and specific humidity:

$$\begin{aligned} &\partial_t s_b' + \nabla \cdot \left[\overline{\mathbf{v}}_b s_b' + \mathbf{v}_b' (s_{rb} + \overline{s}_b) \right] - \overline{s}^{\dagger} \nabla \cdot \mathbf{v}_b' - s^{\dagger\prime} \nabla \cdot \overline{\mathbf{v}}_b \\ &\quad = \frac{g}{p_B} H' + \langle Q_R' \rangle^b + \langle Q_c' \rangle^b + k_q \nabla^2 s_b', \end{aligned} \tag{11}$$

and

$$\begin{aligned} &\partial_t q_b' + \nabla \cdot \left[\overline{\mathbf{v}}_b q_b' + \mathbf{v}_b' (q_{rb} + \overline{q}_b) \right] - \overline{q}^{\dagger} \nabla \cdot \mathbf{v}_b' - q^{\dagger\prime} \nabla \cdot \overline{\mathbf{v}}_b \\ &\quad = \frac{g}{p_B} E' + \langle Q_q' \rangle^b + k_q \nabla^2 q_b', \end{aligned} \tag{12}$$

where s_b is the dry static energy in the ABL and $p_B = p_s - p_e$ is the ABL depth. E and H are the surface fluxes of latent and sensible heat, respectively, and $\langle\ \rangle^b$ indicates averaging over the boundary layer.

[16] For the ABL velocity, the equation is:

$$\begin{aligned} &\partial_t \mathbf{v}_b' + \nabla \cdot \left(\overline{\mathbf{v}}_b \mathbf{v}_b' + \mathbf{v}_b' \overline{\mathbf{v}}_b \right) - \overline{\mathbf{v}}^{\dagger} \nabla \cdot \mathbf{v}_b' - \mathbf{v}^{\dagger\prime} \nabla \cdot \overline{\mathbf{v}}_b + f \hat{\mathbf{k}} \times \mathbf{v}_b' \\ &\quad = -\nabla \left(\kappa \langle a_b^+ \rangle^b s_b' + \phi_s' \right) - \epsilon_b \mathbf{v}_b' + k_v \nabla^2 \mathbf{v}_b', \end{aligned} \tag{13}$$

where ϵ_b is a surface drag coefficient. The coefficient of the baroclinic ABL geopotential contribution $\langle a_b^+ \rangle^b$ results from the integration to obtain the vertical average of geopotential in the ABL:

$$\langle a_b^+ \rangle^b = p_B^{-1} \int_{p_e}^{p_s} \int_{p}^{p_s} a_b \, d\ln p \, dp. \tag{14}$$

[17] In the axisymmetric framework, the continuity equation is:

$$\mu v_b' = -v_0', \tag{15}$$

where $\mu = p_B/p_F$ is the ratio of the depth of the ABL to the depth $p_F = p_e - p_t$ of the free troposphere.

[18] In practice, equations (8) and (13) are combined to eliminate the geopotential gradient $\partial_y \phi_s'$, and the continuity equation (15) is used to eliminate v_b to obtain the following expression for v_0:

$$\begin{aligned} &\partial_t v_0' + 2(1 - \mu^{-1}) (\overline{v}_0 \partial_y v_0' + v_0' \partial_y \overline{v}_0) + 2\tilde{\mu} \langle V_1^2 \rangle (\overline{v}_1 \partial_y v_1' + v_1' \partial_y \overline{v}_1) \\ &\quad - v^{\dagger\prime} \partial_y \overline{v}_0 - \overline{v}^{\dagger} \partial_y v_0' + \tilde{\mu} f (u_0' - u_b') \\ &\quad = -\tilde{\mu} \kappa \, \partial_y \left[\left(a_b^{+e} - \langle a_b^+ \rangle^b \right) s_b' + \langle a_1^+ \rangle T_1' \right] \\ &\quad - \frac{\tilde{\mu}}{\mu} \epsilon_b v_0' + k_v \partial_y^2 v_0', \end{aligned} \tag{16}$$

with $\tilde{\mu} = \mu(1 + \mu)^{-1}$.

[19] The resulting model has 9 prognostic variables: u_1', v_1', u_0', v_0', u_b', T_1', s_b', q_1', and q_b', and the base state is defined by 9 fields $\overline{u}_1$, $\overline{v}_1$, $\overline{u}_0$, $\overline{v}_0$, $\overline{u}_b$, $\overline{T}_1$, $\overline{s}_b$, $\overline{q}_1$, and $\overline{q}_b$. It is essentially equivalent in its overall level of complexity to a three-layer model, with the primary difference being that

the free-tropospheric structure is represented by modes rather than layers. It is comparable in complexity to the models used by *Jiang et al.* [2004] and *Drbohlav and Wang* [2005], with the most substantial differences being the use of a prognostic boundary layer and a number of different choices in the model physics, described below.

2.3. Model Physics

2.3.1. Convection

[20] The convective heating and moistening $\langle Q_c' \rangle$, $\langle Q_c' \rangle^b$, $\langle Q_q' \rangle$, and $\langle Q_q' \rangle^b$ are parameterized using the Betts-Miller scheme [*Betts*, 1986; *Betts and Miller*, 1986] as implemented in the prototype QTCM2 [*Sobel and Neelin*, 2006]. In the Betts-Miller scheme, precipitation is proportional to a quantity similar to the convective available potential energy of the column, here denoted $\mathcal{E}$, if this quantity is positive, and is zero otherwise. To linearize the model, we omit this positive-only precipitation criterion for the perturbation of $\mathcal{E}$. BS showed that this simplification yields linear modes whose properties match those of the original nonlinear limit cycles closely. A sensitivity study using a modified, linearizable version of this criterion also showed that our results are not sensitive to this simplification. The precipitation can be expressed as follows:

$$P' = \epsilon_c \mathcal{E}' = \epsilon_c \left[p_F \langle a_1 \rangle \left(h_b' + \delta h_b' - T_1' \right) + p_B \, \sigma \, \delta h_b' \right], \tag{17}$$

where $\epsilon_c = \tau_c^{-1}$ is a (large) rate for the removal of buoyancy by convection and σ is a parameter that partitions the convective cooling and drying in the boundary layer. $h_b' = s_b' + q_b'$ is the boundary layer perturbation of moist static energy, and $\delta h_b'$ is an adjustment perturbation that accounts for some downdraft effects. $\mathcal{E}$ is not exactly analogous to standard, nonentraining CAPE, as can be seen from its dependence on free-tropospheric moisture. Nonetheless, we refer to $\mathcal{E}$ as the CAPE below, as it does have energy units and plays the role that CAPE does in many convective closures.

[21] The convective contributions to the energy and water budgets are:

$$\begin{aligned} \langle Q_c' \rangle &= \epsilon_c \langle a_1 \rangle \left(h_b' + \delta h_b' - T_1' \right), \\ \langle Q_q' \rangle &= \epsilon_c \langle b_1 \rangle \left(h_b' + \delta h_b' - q_1' \right), \\ \langle Q_c' \rangle^b &= \epsilon_c \, \sigma \, \delta h_b', \\ \text{and} \quad \langle Q_q' \rangle^b &= \epsilon_c \, (1 - \sigma) \, \delta h_b', \end{aligned} \tag{18}$$

$\delta h_b'$ results from the energy constraint that the net moisture loss must equal the net (dry) enthalpy gain and can be written:

$$\delta h_b' = \frac{\left[-(\langle a_1 \rangle + \langle b_1 \rangle) h_b' + \langle a_1 \rangle T_1' + \langle b_1 \rangle q_1' \right]}{\mu + \langle a_1 \rangle + \langle b_1 \rangle}. \tag{19}$$

[22] Combining (17) and (19) yields an expression of $\mathcal{E}'$ as a function of h_b', T_1' and q_1':

$$\mathcal{E}' = \mathcal{E}_b h_b' + \mathcal{E}_q q_1' + \mathcal{E}_T T_1', \tag{20}$$

with

$$\begin{aligned} \mathcal{E}_b &= p_B \frac{\langle a_1 \rangle (1 - \sigma) - \langle b_1 \rangle \sigma}{\mu + \langle a_1 \rangle + \langle b_1 \rangle}, \\ \mathcal{E}_q &= p_F \langle b_1 \rangle \frac{\langle a_1 \rangle + \sigma \mu}{\mu + \langle a_1 \rangle + \langle b_1 \rangle}, \\ \text{and} \quad \mathcal{E}_T &= -p_F \langle a_1 \rangle \frac{\langle b_1 \rangle + (1 - \sigma) \mu}{\mu + \langle a_1 \rangle + \langle b_1 \rangle} \end{aligned}$$

2.3.2. Radiation

[23] We use a Newtonian relaxation in the free troposphere and in the boundary layer, with a shorter timescale for the ABL:

$$\langle Q_R' \rangle = -\frac{T_1'}{\tau_R} \quad \text{and} \quad \langle Q_R' \rangle^b = -\frac{s_b'}{\tau_{Rb}} \tag{21}$$

2.3.3. Surface Fluxes

[24] Surface fluxes are parameterized by linearized standard bulk formulae:

$$E' = \rho_a C_D \left[\overline{\mathbf{v}}_b \cdot \mathbf{v}_b' \, \mathrm{V}_s^{-1} (q^*(T_s) - \overline{q}_b) - \mathrm{V}_s q_b' \right] \tag{22}$$

$$H' = \rho_a C_D \left[\overline{\mathbf{v}}_b \cdot \mathbf{v}_b' \, \mathrm{V}_s^{-1} (T_s - \overline{s}_b) - \mathrm{V}_s s_b' \right] \tag{23}$$

where T_s is the SST, $q^*(T_s)$ is the saturation specific humidity at T_s, C_D is the exchange coefficient, ρ_a is the surface air density, and V_s is the mean surface wind speed:

$$\mathrm{V}_s = \sqrt{G^2 + |\overline{\mathbf{v}}_b|^2}, \tag{24}$$

where G is the gustiness, a constant wind that accounts for subgrid circulations. The first term in the brackets of equations (22) and (23) is the wind-induced surface heat flux that was shown to be crucial to the modeled intraseasonal oscillation in BS.

2.4. Computation Design and Control Case

[25] The equations of the model are discretized over a domain of 20.000 km (10.000 km in each hemisphere), with a spatial resolution of 50 km (400 grid points). The Jacobian matrix of the model is computed, using a specified mean state. The eigenvalues and eigenvectors are then numerically computed. Only the unstable modes, if any, are described in this study. In such a mode, the time evolution of the precipitation can be expressed as follows:

$$P'(y,t) = \mathcal{R}e\left\{ N_P(y) e^{\lambda t} \right\} = \mathcal{A}_P(y) \cos\left(2\pi \frac{t}{\mathcal{T}} - \phi_P(y) \right) e^{\frac{t}{\tau_e}}, \tag{25}$$

where $N_P(y)$ is the precipitation component of the complex eigenmode and λ is the associated complex eigenvalue (with positive imaginary part). $\mathcal{A}_P = |N_P|$ is the precipitation amplitude, $\phi_P = -arg(N_P)$ is its phase. $\mathcal{T} = 2\pi/\mathcal{I}m(\lambda)$ is the period of the mode and $\tau_e = 1/\mathcal{R}e(\lambda)$ is its e-folding time. Note that the amplitude $\mathcal{A}_P(y)$ can be rescaled simply by changing the time origin, and thus contains information only on the latitudinal structure of the mode. This structure

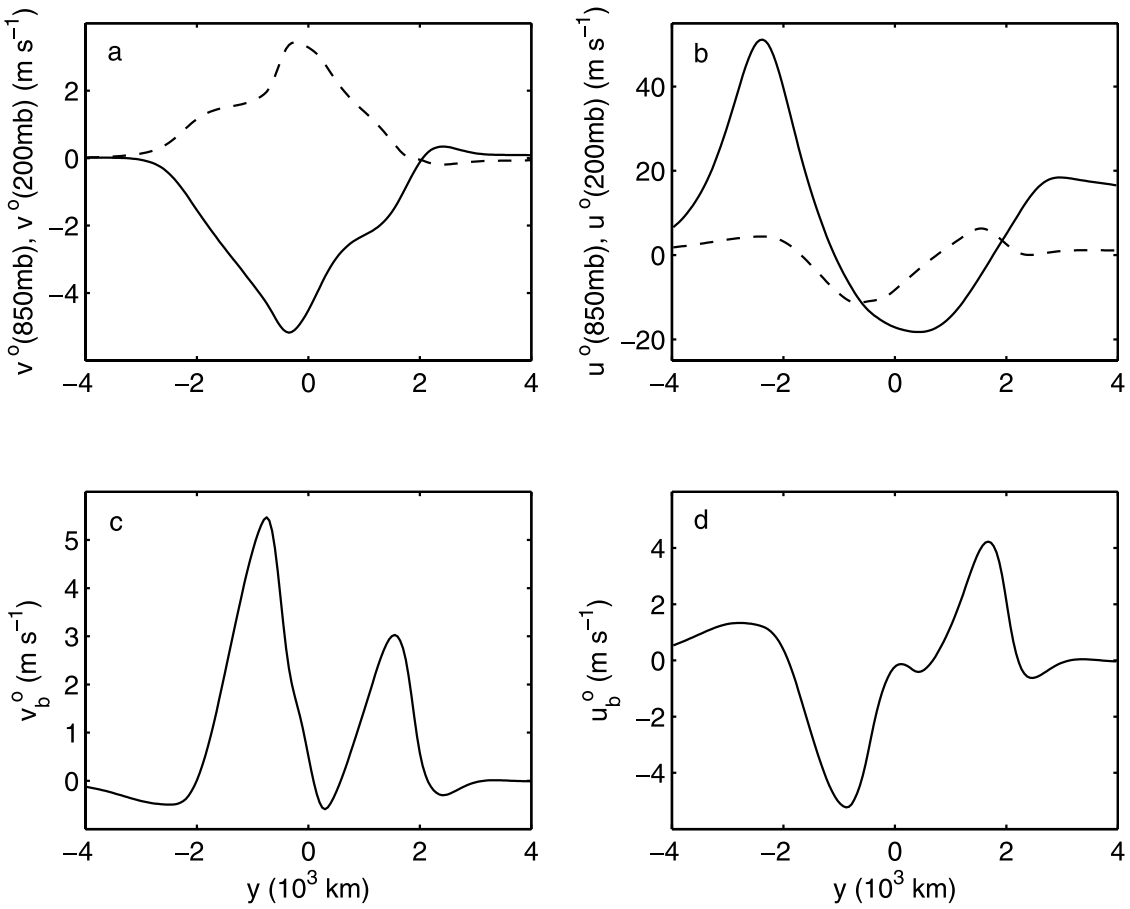

Figure 1. Mean state of the model in the control case: (a) meridional wind at 200 mbar (solid) and 850 mbar (dashed), (b) zonal wind at 200 mbar (solid) and 850 mbar (dashed), (c) ABL meridional wind and (d) ABL zonal wind (solid).

is also described by $\phi_P(y)$ that provides information on the phase differences between latitude, and therefore the propagation; it is counted positively for a lag so that an increase of ϕ_P with latitude corresponds to a northward propagation.

[26] In the control case, the base state is taken as the time mean over the first limit cycle of the nonlinear model described in BS (in particular, the nonlinear model uses the positive-only precipitation criterion in the Betts-Miller parameterization). This mean state is shown in Figures 1 and 2 (see also Figures 1–3 in BS). The control SST is uniform, with a value of 29°C between the equator and 2000 km north of it (which corresponds to the northern limit of the Bay of Bengal and the Arabian Sea), and is a sinusoid north of there and in the Southern Hemisphere, as shown in Figure 2b. The control base state and SST are denoted by the superscript circle.

[27] Table 1 shows the parameters used in the control case, which are very similar to the parameters used in BS. As 1° of latitude roughly equals 100 km, the latitude will be either given in degrees or kilometers.

[28] In BS we showed that the model has one linearly unstable, oscillatory mode in the control state. Here, this oscillation has a period of 55.2 d and an *e*-folding growth time of 54.3 d. This result differs slightly from that in BS because of minute modifications of the model's parameters. Figure 3 shows the time evolution of precipitation anomalies for the nonlinear model and the oscillatory component of the precipitation in the unstable linear mode $\mathcal{A}_P(y)\cos(2\pi t/\mathcal{T} - \phi_P(y))$. The unstable linear mode exhibits the same structure and space and timescales as does the oscillation in the nonlinear model and as does the 30–60 d oscillation of the atmosphere over south Asia during the monsoon. It is characterized by northward propagation of precipitation anomalies between the equator and 25°N, with two maxima of precipitation amplitude colocated with the equatorial and monsoonal TCZs of the mean state (BS).

[29] The similarity of the structures in the linear and nonlinear calculations shows that the dynamics of the oscillation in the model is essentially linear. The linear model allows one to study the influence of parameter changes on the oscillation independently of their influence on the mean state. In Appendix A, we show the sensitivity of the oscillation to several parameters. The results are not inherently of great interest, but do demonstrate that the period of the unstable mode, in particular, is not very sensitive to parameters. Its stability is somewhat more sensitive, a fact which we use later as described in section 4.2. The role of the basic state in the

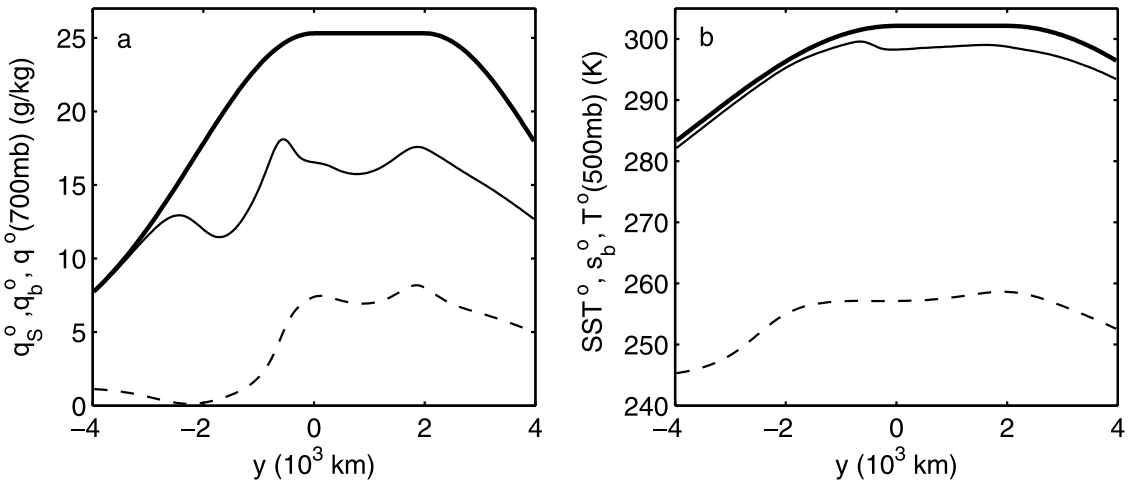

Figure 2. Mean state of the model in the control case: (a) saturation humidity at the SST (thick), ABL humidity (solid) and free-tropospheric humidity (at 700 mbar, dashed); (b) SST (thick), ABL (solid) and free-tropospheric (at 500 mbar, dashed) temperatures.

development of the oscillation can also be investigated using the linear model. This is the subject of the next section.

3. Sensitivity to the Mean State

[30] In previous studies, the role of the structure of the mean state has been highlighted. Some studies have concluded that the thermodynamic aspects of the mean state are crucial in determining the northward propagation of convection [*Nanjundiah et al.*, 1992]. Other studies have proposed mechanisms associated with the mean monsoon flow [*Jiang et al.*, 2004; *Drbohlav and Wang*, 2005]. Here, we explore the influence of the mean fields on the stability or instability of the mean flow and on the structure and scale selection of the intraseasonal mode by varying the base state, regardless of the physical consistency of the resulting mean flow.

[31] The results of this strategy must be interpreted with care. When we study linear perturbations to a basic state which is not a solution of the underlying nonlinear equations, we violate the premises of linear perturbation theory. (Strictly, we have already violated those premises by taking as our base state the time mean from a nonlinear calculation whose evolution is unsteady, rather than a true time-independent state.) We view such calculations as a way of quantifying the importance of different terms to the instability; removing them from the computation of eigenvalues is arguably a more relevant way of doing this than simply comparing different terms in a budget. Also, the ends justify the means in some of the calculations. If a removal of all structure in a particular basic state field results in

Table 1. Model Parameter Values

Parameter	Value	Definition
p_s, p_e, p_t	1000, 900, 150 hPa	pressures at nominal surface, ABL top, and model top
$\langle a_1 \rangle$, a_{1e}	0.4243, 0.2931	vertical mean and ABL top value of temperature basis function
$\langle b_1 \rangle$, b_{1e}	0.2406, 07576	vertical mean and ABL top value of moisture basis function
$\langle a_1^+ \rangle$	0.2445	
$\langle a_b^+ \rangle^b$, a_b^{+e}	0.0512, 0.1038	
$\langle V_1^2 \rangle$, $\langle V_1^3 \rangle$	3.67×10^{-2}, 3.2×10^{-3}	
V_{1e}	−0.2121	ABL top value of baroclinic basis function
q_{re}, T_{re}	38.925 K, 296.65 K	ABL top reference moisture and temperature
q_{rb}, s_{rb}	51.96 K, 302.00 K	ABL reference moisture and dry static energy
M_{sr1}, M_{sr0}	3.60 K, 16.34 K	reference dry static stabilities
M_{sp1}, M_{sp0}	4.05×10^{-2}, 0.188	dry static stability changes per T_1 change
M_{qr1}, M_{qr0}	3.00 K, 28.05 K	reference gross moisture stratifications
M_{qp1}, M_{qp0}	3.78×10^{-2}, 0.516	gross moisture stratification changes per q_1 change
ϵ_1	8.77×10^{-7} s^{-1}	frictional damping rate on baroclinic mode
ϵ_b	2.20 10^{-5} s^{-1}	ABL drag coefficient
τ_c	0.3 d	convective timescale
σ	0.2	constant partitioning between convective cooling and drying of ABL
T_R, τ_R	−50 K, 15 d	radiative equilibrium temperature and timescale
Q_{Rb0}, τ_{Rb}	−1.5 K d^{-1}, 2 d	ABL radiative background heating and timescale
ρ_a, C_D	1 kg m^{-3}, 1.5×10^{-3}	surface air density, exchange coefficient
k_q, k_v	8×10^5, 2×10^5 m^2 s^{-1}	diffusivities for moisture and velocity

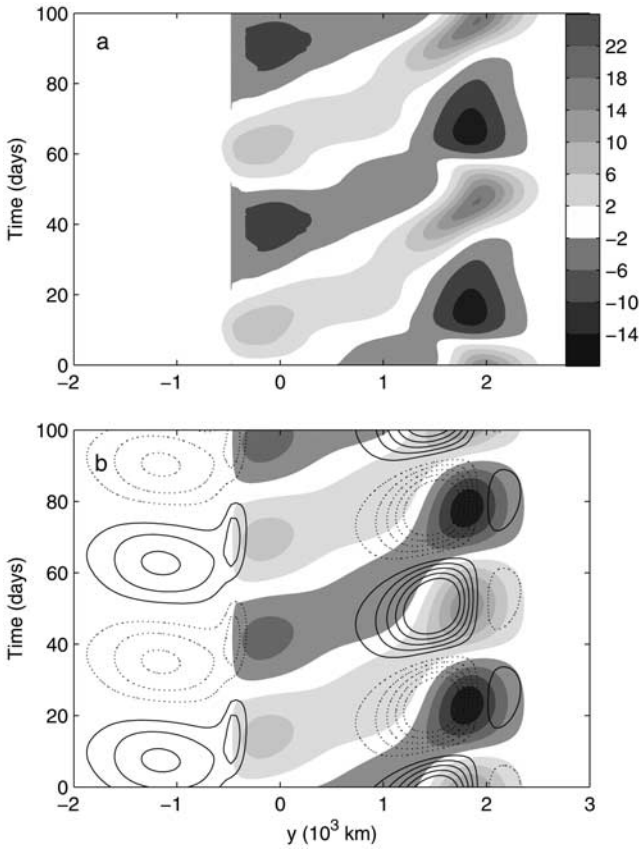

Figure 3. Shading indicates precipitation anomaly in the (a) nonlinear and (b) linear oscillations. Contours indicate surface-heat-flux anomaly in the linear oscillation (solid contours for positive values and dashed for negative values).

little change to the computed unstable mode, we feel justified in claiming that the removed structure is not important to the mode's dynamics in the control case.

3.1. Sensitivity to the Mean Thermodynamic Fields

[32] We suppress the influence of the spatial structure in the mean thermodynamic fields by setting them to uniform, typical tropical values over the whole domain: $SST = 29°C$, $\overline{s}_b = 299$ K, $\overline{T}(500\text{ mb}) = 258$ K, $\overline{q}_b = 16$ g/kg, $\overline{q}(700\text{ mb}) = 8$ g/kg. The dynamical fields $\overline{\mathbf{v}}_0$, $\overline{\mathbf{v}}_1$, and $\overline{\mathbf{v}}_b$ are set to the control values $\mathbf{v}_0^\circ$, $\mathbf{v}_1^\circ$, and $\mathbf{v}_b^\circ$. We call this experiment Case FlatqT.

[33] The base state of FlatqT is linearly unstable, and the one unstable mode is oscillatory, with an e-folding time $\tau_e = 28.3$ d and a period $\mathcal{T} = 54.9$ d. Figure 4 shows the mode's amplitude $\mathcal{A}_P$ and phase ϕ_P. Compared to the control case, this mode is about twice as unstable, and it has a very similar period, and a somewhat similar structure. The equatorial maximum of $\mathcal{A}_P$ is strengthened and the mode extends into the Southern Hemisphere where an additional maximum appears around 15°S (Figure 4a). These changes result primarily from the increased variability of the surface fluxes south of the equator due to higher SSTs there than in the control case. These increased surface fluxes are associated with a moisture feedback: increased mean gross moisture stratifications $\overline{M}_{q0}$ and $\overline{M}_{q1}$ allow an efficient moistening of the free troposphere with ascending motion, and this moistening sustains the convection by increasing the CAPE. Removing the mean thermodynamic gradients does not affect the northward propagation: ϕ_P increases with increasing latitude (Figure 4b), in a very similar way to the control case in the Northern Hemisphere.

[34] In our model, the main roles of the mean horizontal structure in the thermodynamic fields are to reduce the instability and to limit the extent of the latitudinal domain in which convection can occur. Convection in the northern tropics is possible because of the high SST there, as it is observed in reality [*Gadgil et al.*, 1984; *Graham and Barnett*, 1987]. Removing the mean thermodynamic gradients while maintaining an SST and a vertical stratification that allow convection does not alter the scale selection, and only marginally modifies the structure of the mode in the region of interest. These gradients have a role in establishing the basic-state circulation, and therefore an indirect role in the intraseasonal mode, but the basic-state circulation appears to have a larger impact on this mode than the basic-state thermodynamic structure. This result contrasts with those of previous studies [*Gadgil and Srinivasan*, 1990; *Nanjundiah et al.*, 1992] in which the mean meridional gradient of a "convective intensity factor" measuring the stability of the atmosphere was essential to the northward propagation.

3.2. Sensitivity to the Mean Flow

[35] We investigate the role of the mean flow by performing the same eigenvalue analysis with a base state where we set to zero the barotropic zonal wind ($\overline{u}_0 = 0$, Case Nou_0), the baroclinic zonal wind ($\overline{u}_1 = 0$, Case Nou_1), the baroclinic meridional wind ($\overline{v}_1 = 0$, Case Nov_1), the ABL zonal wind ($\overline{u}_b = 0$, Case Nou_b), or the ABL meridional wind ($\overline{v}_b = 0$, Case Nov_b), keeping all the other mean fields as in the control case. In the last case, for consistency, the mean meridional barotropic wind is zero.

[36] Table 2 sums up the results for the different cases. In cases Nov_1, Nou_b, and Nov_b, the base state is stable: the meridional mean flow in the free troposphere and both components of the ABL mean flow appear necessary to the development of an oscillation. In Case Nou_0, the base state is unstable, and the characteristic times of the unstable mode are very similar to the control case: $\mathcal{T} = 58.3$ d and $\tau_e = 47.3$ d. In case Nou_1, the base state is unstable as well, but the period is about 20% larger, and the e-folding time is much larger than in the control case: $\mathcal{T} = 65.9$ d and $\tau_e = 334.1$ d. The precipitation structure of these modes are shown in Figure 4. Neglecting $\overline{u}_0$ or $\overline{u}_1$ only marginally modifies the structure of the mode: ϕ_P increases with latitude in a similar way as in the control case (Figure 4b) and the monsoonal maximum of $\mathcal{A}_P$ is clearly visible (Figure 4a). The equatorial maximum of $\mathcal{A}_P$ is smoother in Case Nou_0 and larger in Case Nou_1. In Case Nou_0, the phase reversal around 25°N has a different sign than in the other cases, and the phase north of this latitude is therefore larger than in the other cases by 2π. These small differences in structure result from modifications in the budget of zonal barotropic momentum. The impact of neglecting the mean zonal shear $\overline{u}_1$ on the stability and period of the oscillation suggests that the "vertical shear mechanism" described by *Jiang et al.* [2004] is at play in our model. This mechanism

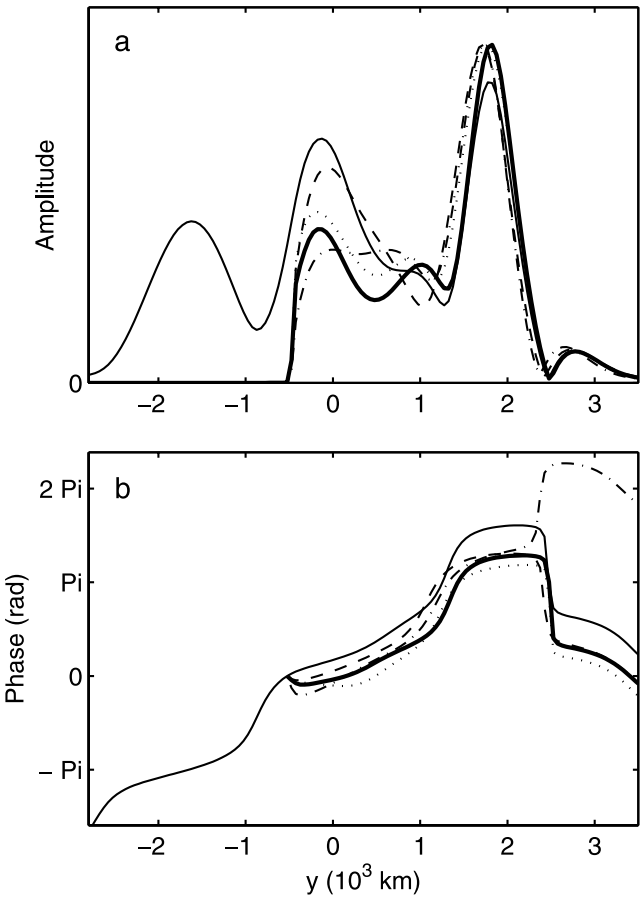

Figure 4. Precipitation amplitude and phase of the unstable mode in the control case (thick line) and for Case FlatqT (solid), Case Nou_0 (dash-dotted), Case Nou_1 (dashed), and Case No$\mathbf{v}_b$exV_s (dotted). Positive phase difference indicates a lag.

increases the instability of the base flow and accelerates the northward propagation.

[37] In our model, the mean ABL flow contributes to the advection terms and the wind-induced surface heat fluxes. The latter were shown to be vital to the instability of the mean flow in our model (BS). To investigate the role of the former, we perform another experiment, with the mean ABL flow set to zero except in the expression of surface fluxes where it is set to those in the control value: $V_s^2 = G^2 + \mathbf{v}_b^{\circ 2}$ and $\overline{\mathbf{v}}_b \cdot \mathbf{v}_b' = \overline{\mathbf{v}}_b^{\circ} \cdot \mathbf{v}_b'$ (in equations (22) and (23)). The other mean fields are set to their control values. This case is noted No$\mathbf{v}_b$exV_s. This base state is linearly unstable, with its one unstable mode characterized by an e-folding time of 94.5 d and a period of 58 d. The structure of this mode is shown in Figure 4. $\mathcal{A}_P$ and ϕ_P are almost identical to their counterparts in the control case. The advective contributions of the control mean ABL flow only accelerate the growth of the unstable mode. In the TCZs, the divergent component of this flow propagates the anomalies of humidity from the ABL to the free troposphere, where they have a stronger impact on the CAPE. This mechanism favors the enhancement of convection over positive anomalies of ABL moisture and constitutes a positive feedback that accounts for most of the destabilizing effect of advection by the mean ABL flow.

[38] In summary, in our model, the only elements of the control base state that are necessary to generate its instability and the main characteristics of the intraseasonal mode in the northern tropics are the mean baroclinic meridional flow and the effect of the mean surface wind on the surface heat fluxes. On the other hand, the advection associated with the mean ABL flow has a modest impact on the unstable mode, increasing its instability, and the mean barotropic flow in the free troposphere is unimportant. The mean baroclinic zonal flow significantly strengthens the instability and accelerates

Table 2. Stability of the Modified Base State and Characteristics of the Unstable Mode, If Any[a]

Run	Stability	$\mathcal{T}$ (days)	τ_e (days)
Ctrl	unstable	55.2	54.3
FlatqT	unstable	54.9	28.3
Nou_0	unstable	58.3	47.3
Nou_1	unstable	65.9	334.1
Nov_1	stable	/	/
Nou_b	stable	/	/
Nov_b	stable	/	/
No$\mathbf{v}_b$exV_s	unstable	58.0	94.5
v_1&$\mathbf{v}_b$inV_s	unstable	62.1	57.5

[a]Slashes mean "not applicable."

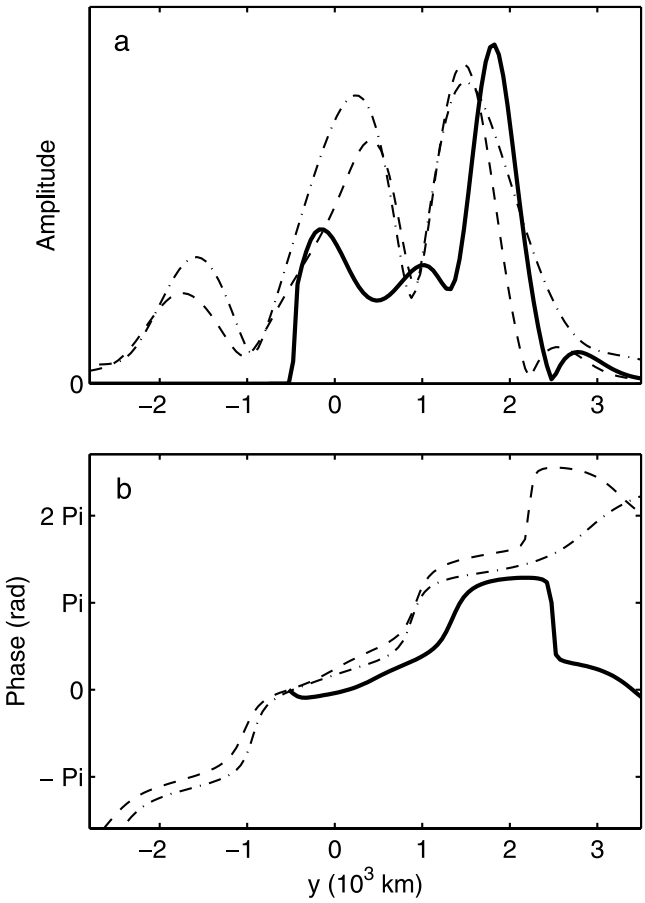

Figure 5. Precipitation amplitude and phase of the unstable mode in the control case (thick line), for Case v_1&$\mathbf{v}_b$inV_s (dashed) and in the control case of the stripped-down model (dash-dotted).

the northward propagation. We now investigate whether the mean baroclinic meridional flow and the effect of the mean surface wind on the surface fluxes are sufficient to obtain an unstable mode. We perform another computation where we set the thermodynamic fields to the flat values used in Case FlatqT and we set to zero all the components of the base flow except the meridional baroclinic wind and the ABL flow in the computation of surface fluxes, both of which are set to the control values. In this case (noted $v_1\&\mathbf{v}_b\text{in}V_s$), the base state has one unstable mode. This mode has a period of 62.1 d and an e-folding time of 57.5 d; its structure in precipitation is shown in Figure 5. This mode is similar to the one obtained in the control case, with a slightly longer period of about two months and with one near-equatorial $\mathcal{A}_P$ maximum and another $\mathcal{A}_P$ maximum in the monsoonal TCZ. The differences in the structure seem to result from a linear addition of the differences obtained in the previous sensitivity experiments: an additional maximum of amplitude appears in the Southern Hemisphere, like in Case FlatqT. The northward shift of the equatorial maximum of $\mathcal{A}_P$ and the southward shift of the monsoonal maximum result from neglecting of $\overline{u}_0$ and $\overline{u}_1$. The gain in instability resulting from neglecting the mean thermodynamic gradients compensates for the stabilization due to removing $\overline{u}_1$ and $\overline{\mathbf{v}}_b$.

[39] The main characteristics of the intraseasonal oscillation in our model (the double maximum of precipitation amplitude north of 10°S and the northward propagation) appear to be primarily controlled by the combination of the advection by the mean baroclinic meridional wind and the effect of the mean surface flow on the surface fluxes. We use these properties to simplify the model in the next section.

4. Stripped-Down Model

4.1. Model Description and Basic Results

[40] In this very simple linear model, we neglect all the mean thermodynamic gradients and the mean flow except for the mean baroclinic meridional wind and the effect of the zonal ABL flow on the surface fluxes. We make the following further simplifications:

[41] 1. Sensitivity studies (not shown) suggest that the tropical average value of $\overline{v}_1$ is the determinant factor feature of $v_1^\diamond$. In particular, the unstable mode appears insensitive to the vertical motion associated with the mean baroclinic divergence $\partial_y\overline{v}_1$. The meridional mean flow is thus set to a constant, the median value of the control case: $\overline{v}_1 = \mathcal{V}_1 = -8$ ms^{-1} [corresponding to $\overline{v}$(850 mb) = -2 ms^{-1} and $\overline{v}$(200 mb) = 2.5 ms^{-1}].

[42] 2. Other sensitivity studies (not shown) show that the unstable mode is not very sensitive to the intensity and latitudinal structure of the trade winds in the Southern Hemisphere. The surface mean zonal flow is thus idealized by a Gaussian function that represents only the mean westerlies in the northern tropics:

$$\overline{u}_b = U_s \cdot \exp\left(-\left[\frac{y-y_u}{\sigma_u}\right]^2\right) \tag{26}$$

with $U_s = 4$ ms^{-1}, $y_u = 1000$ km and $\sigma_u = 500$ km in the control case. This wind is taken into account in the computation of the surface fluxes only, as in Case No$\mathbf{v}_b$exV_s.

[43] 3. The anomalies of CAPE associated with surface moisture and dry static energy anomalies are small in all the cases described in the previous sections. We thus neglect these anomalies q_b' and s_b', so the equations for vertically integrated energy and humidity become:

$$\begin{aligned}\langle a_1\rangle\partial_t T_1' + \left(\nabla\cdot\mathbf{v}_0'\right)\left(\langle\overline{s}\rangle - s_{rb} - \overline{s}_b\right) + \langle a_1 V_1\rangle\overline{\mathbf{v}}_1\cdot\nabla T_1' \\ + \overline{M}_{s1}\left(\nabla\cdot\mathbf{v}_1'\right) = \frac{g}{p_F}H' + \langle Q_c'\rangle + \mu\langle Q_c'\rangle^b + \langle Q_R'\rangle \\ + \langle a_1\rangle k_q\nabla^2 T_1',\end{aligned} \tag{27}$$

and

$$\begin{aligned}\langle b_1\rangle\partial_t q_1' + \left(\nabla\cdot\mathbf{v}_0'\right)\left(\langle\overline{q}\rangle - q_{rb} - \overline{q}_b\right) + \langle b_1 V_1\rangle\overline{\mathbf{v}}_1\cdot\nabla q_1' \\ - \overline{M}_{q1}\left(\nabla\cdot\mathbf{v}_1'\right) = \frac{g}{p_F}E' + \langle Q_q'\rangle + \mu\langle Q_q'\rangle^b + \langle b_1\rangle k_q\nabla^2 q_1',\end{aligned} \tag{28}$$

Here, we have included the previous simplifications and used $\langle Q_R'\rangle^b = 0$.

[44] This last simplification at first seems somewhat at odds with experiment Tq_b in BS. In that experiment, the perturbation ABL humidity was tied to the free-tropospheric perturbation ($q_b' \propto q_1'$) and the base state was stable. We concluded that the second degree of freedom in the vertical structure of humidity was necessary to the instability. Here, we actually suppress variations in ABL moisture, and the base state remains unstable. We interpret these two results as indicating that the second degree of freedom in the vertical structure of the humidity is important in that it allows variations of q_1 independently of q_b, but that the variations of q_b itself are not crucial.

[45] In this control configuration (Case Ctrl), the instability is enhanced: $\tau_e = 20.9$ d and the unstable mode has a period of 65.4 d. Figure 5 shows the structure of the mode. This case is very similar to Case $v_1\&\mathbf{v}_b\text{in}V_s$ of the previous section, except for the shorter e-folding time. This shows that the simplifications of the stripped-down model do not significantly alter the structure of the oscillation. The increased instability is explained by the modification of the hydrological cycle: by neglecting the ABL humidity anomalies, all humidity anomalies are concentrated in the free troposphere. Since the CAPE $\mathcal{E}$ is more sensitive to the free-tropospheric humidity than to the ABL humidity, this enhances the variations of $\mathcal{E}'$ and reinforces the moisture-convergence feedback on convection.

[46] The double maximum of precipitation amplitude (over the equator and the northern tropics) and the northward propagation of the anomaly can therefore be accounted for by two simple elements of the base state: a constant mean baroclinic meridional wind and wind-induced surface fluxes associated with westerlies in the northern tropics. Setting either U_s or $\mathcal{V}_1$ to zero stabilizes the base state.

4.2. Respective Roles of $\mathcal{V}_1$ and U_s

[47] In order to distinguish between the role of the surface wind and that of the meridional baroclinic flow, one would like to set U_s and/or $\mathcal{V}_1$ to zero and study the changes in the

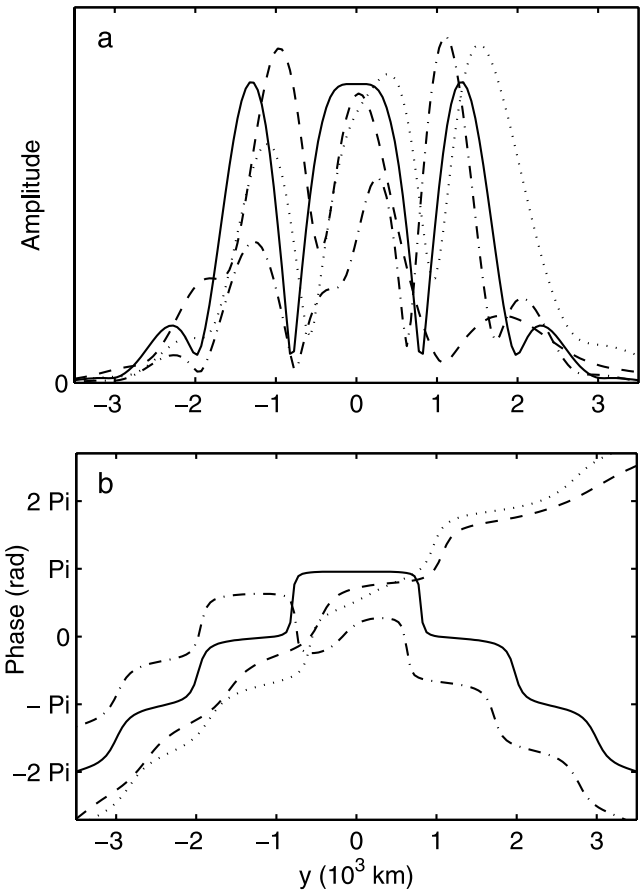

Figure 6. Precipitation amplitude and phase of the unstable mode for Case No$\mathcal{V}_1 U_s$ (solid), for Case No$\mathcal{V}_1$ (dash-dotted), for Case NoU_s (dashed), and in the control case Ctrl' (dotted).

mode that is unstable in the control case. Unfortunately, it is impossible to do this while keeping the model parameters fixed. The formerly unstable mode, when stabilized by the removal of $\mathcal{V}_1$ or U_s, does not turn into the least stable mode of the modified system, because other weakly stable modes are not sensitive to U_s nor $\mathcal{V}_1$. These other modes become the least stable modes when U_s or $\mathcal{V}_1$ is set to zero. The unstable mode of the control case is then impossible to distinguish among the 2802 stable eigenmodes of the Jacobian matrix.

[48] Therefore, to study the respective roles of U_s and $\mathcal{V}_1$, we use the model sensitivity to its parameters in order to increase the instability so that the base state of the stripped-down model is unstable even when U_s and/or $\mathcal{V}_1$ are set to zero. We use the sensitivity study to the model's parameters (see Appendix A) to choose modified radiative and convective timescales: τ_c = 0.15 d and τ_R = 30 d. With these modified parameters (Case Ctrl′) and the same values of U_s and $\mathcal{V}_1$ as used previously, the unstable mode has a period of 85 d and an *e*-folding time of 11.9 d. Figure 6 shows the structure of the mode. Despite the longer period, the unstable mode is similar to Case Ctrl, featuring two maxima of amplitude and northward propagation.

[49] We perform three sensitivity computations: one with no surface westerlies (Case NoU_s), one with no baroclinic base flow (Case No$\mathcal{V}_1$) and one with both $\overline{v}_1$ and $\overline{u}_b$ set to zero (Case No$\mathcal{V}_1$ U_s). All three cases are unstable thanks to the choice of radiative and convective timescales. The properties of the unstable modes are displayed in Table 3. The structures of these modes are shown in Figure 6.

[50] In Case No$\mathcal{V}_1$ U_s, the unstable mode features three maxima of precipitation amplitude, one equatorial maximum and two off-equatorial symmetric maxima. The distance between these maxima and the equator is about one equatorial radius of deformation. The phase reversal between the equatorial maximum and the off-equatorial maxima shows that this mode is an oscillation between a single and a double Intertropical Convergence Zone (ITCZ; we consider them as two particular types of TCZs). The *e*-folding time and period of this mode are twice as long as those in the control case Ctrl′. Case No$\mathcal{V}_1$ is similar to Case No$\mathcal{V}_1$ U_s; the main difference between these two cases is the amplitude of the northernmost maximum of precipitation, which is significantly larger than those of the two other maxima. Case NoU_s is similar to the control case in terms of the northward propagation and the period in the intraseasonal range (with a somewhat shorter period than in the control case). This implies that the mean meridional baroclinic flow is the main factor that sets the direction of the propagation and its period. The *e*-folding time is much longer in Case NoU_s than in the Case Ctrl′. This shows that the wind-induced surface fluxes are a major contributor to the instability of the base flow, a result in keeping with that of the previous section and of experiment NoW in BS.

[51] In terms of latitudinal modulation of the precipitation amplitude, it appears that the three-maximum structure is intrinsic to the model regardless of the mean flow. The spatial scale of the northward propagation is therefore primarily set by the equatorial radius of deformation. Nevertheless, the magnitudes and exact location of the maxima are modulated by the mean flow. In Case NoU_s, the precipitation amplitude is larger in the southern tropics, while it is larger in the northern tropics in the Case Ctrl' as well as in Case No$\mathcal{V}_1$. The mean meridional baroclinic wind tends to concentrate the oscillation in the Southern Hemisphere while the wind-induced surface fluxes favor the Northern Hemisphere. Case Ctrl′ suggests that the latter effect is dominant.

5. Mechanisms of Instability and Propagation

[52] We perform an additional experiment in which we neglect the mean free-tropospheric advection of anomalous dry static energy and humidity in the stripped-down model ($\overline{v}_1$ = 0 in equations (27) and (28)). The base state is unstable in this case too, and the mode is very similar to Case Ctrl north of 10°S. This result shows that the mechanisms that cause the instability of the mean flow and the

Table 3. Period and *e*-Folding Time of the Stripped-Down Model

Run	$\mathcal{T}$ (days)	τ_e (days)
Ctrl	65.4	20.9
Ctrl'	85.0	11.9
NoU_s	60.1	45.9
No$\mathcal{V}_1$	134.	17.7
No$\mathcal{V}_1 U_s$	161.	19.2

intraseasonal oscillation in our model are essentially dynamical. In particular, it shows that "moisture-convection feedback mechanism" described by *Jiang et al.* [2004] is not active in our model.

[53] To study the mechanisms of the stripped-down model, it is useful to recognize that in this model divergence tendencies of the barotropic and baroclinic modes are quite simple. By differentiating equations (16) and (9) with respect to latitude and taking into account the defining properties of this model given in section 4.1, one finds:

$$\partial_t D_0' + 2\tilde{\mu}\langle V_1^2\rangle \mathcal{V}_1 \partial_y D_1' - \frac{V_{1e}}{2}\mathcal{V}_1 \partial_y D_0' + \tilde{\mu}\partial_y\left[f\left(u_0' - u_b'\right)\right] = -\tilde{\mu}\langle a_1^+\rangle \kappa\, \partial_y^2 T_1' - \frac{\tilde{\mu}}{\mu}\,\epsilon_b D_0' + k_v \partial_y^2 D_0' \tag{29}$$

and

$$\partial_t D_1' + \frac{3}{2}\mathcal{V}_1 \partial_y D_0' + \frac{3\langle V_1^3\rangle}{2\langle V_1^2\rangle}\mathcal{V}_1 \partial_y D_1' + \partial_y\left(f u_1'\right) = -\kappa \partial_y^2 T_1' - \epsilon_1 D_1' + k_v \nabla^2 D_1', \tag{30}$$

where $D_0' = \partial_y v_0'$ is the barotropic divergence (i.e., divergence in the free troposphere and convergence in the boundary layer) and $D_1' = \partial_y v_1'$ is the baroclinic divergence (i.e., divergence in the upper troposphere end convergence in the lower free troposphere).

[54] The equations for zonal velocities are also very simple in this version of the model:

$$\partial_t u_0' = -\langle V_1^2\rangle \mathcal{V}_1 \partial_y u_1' + f v_0' + k_v \partial_y^2 u_0', \tag{31}$$

$$\partial_t u_1' = -\mathcal{V}_1 \partial_y u_0' - \frac{\langle V_1^3\rangle}{\langle V_1^2\rangle}\mathcal{V}_1 \partial_y u_1' + f v_1' - \epsilon_1 u_1' + k_v \partial_y^2 u_1', \tag{32}$$

$$\text{and } \partial_t u_b' = f v_b' - \epsilon_b u_b' + k_v \partial_y^2 u_b'. \tag{33}$$

5.1. Slow Mechanism of Oscillation: Coriolis Acceleration

[55] In Cases No$\mathcal{V}_1 U_s$ and No$\mathcal{V}_1$, in the absence of mean meridional baroclinic wind, the divergences are controlled by the deviations from geostrophic balance:

$$\partial_t D_0' \approx -\tilde{\mu}\left(\partial_y\left[f\left(u_0' - u_b'\right)\right] + \langle a_1^+\rangle \kappa\, \partial_y^2 T_1'\right) \tag{34}$$

$$\text{and } \partial_t D_1' \approx -\partial_y\left(f u_1'\right) - \kappa \partial_y^2 T_1'. \tag{35}$$

Convection warms the free troposphere. The term in the Laplacian of T_1' therefore tends to enhance both the barotropic and baroclinic divergences at the latitude of maximum convection. These terms can be thought of as the agents in the momentum budgets by which the close instantaneous association between heating and divergence is generated. On the contrary, the gradient of the Coriolis acceleration drives the oscillation. The mechanism of this oscillation is represented in Figure 7. Let us consider a TCZ over the equator. A Hadley-type circulation develops in the tropical atmosphere, with westerlies in the free troposphere and easterlies in the boundary layer (Figure 7a). Further away from the equatorial forcing, the zonal winds u_0', u_1', and u_b' decrease to zero and the Coriolis accelerations for both barotropic and baroclinic meridional winds ($-\tilde{\mu} f(u_0' - u_b')$ and $-f u_1'$) have minima in the northern tropics and maxima in the southern tropics (Figure 7b). Following equations (34) and (35), their contributions to the tendencies of the barotropic and baroclinic divergence damp the divergence at the equator and create divergence away from the equator (Figure 7c). This dynamically induced divergence drives convection away from the equator (Figure 7d).

[56] Conversely, a double ITCZ situation creates a cyclonic circulation in each hemisphere with westerlies in the ABL and easterlies in the free troposphere equatorward of both convergence zones. This configuration is opposite to the one represented in Figures 7a and 7b and the meridional gradients of the Coriolis accelerations, dominated by the vorticity effect $f\zeta_i'$ away from the equator ($\zeta_i' = -\partial_y u_i'$) and by the beta effect $-\beta u_i'$ near the equator, damp barotropic and baroclinic divergence away from the equator while creating divergence at the equator. This damps the double ITCZ and drives convection at the equator. This Coriolis-driven symmetric mechanism gives rise to a 161-d oscillation; compared to the intraseasonal timescales, it is a slow mechanism.

[57] The fundamental result of this experiment is that the three-maximum structure of the precipitation exists in the absence of basic flow. Although the basic flow does alter the latitudinal modulation of the precipitation amplitude, the spatial scale of the propagation seems to be set primarily by this three-maximum structure, with off-equatorial maxima at about one equatorial radius of deformation from the equator.

[58] The amplitude of variability in precipitation is modified by the mean meridional baroclinic flow. In Case NoU_s, the precipitation amplitude is larger in the Southern Hemisphere, and although intricate feedbacks intervene in the latitudinal modulation of amplitude in this case, the primary influence of $\mathcal{V}_1$ arises from the modification of the mechanism described above. If we introduce a negative mean meridional wind $\mathcal{V}_1 < 0$, the profiles of the zonal winds in Figure 7b are shifted southward by the mean advection of anomalous momentum (i.e., by the advective terms in equations (31) and (32)). As a result, the Coriolis acceleration is more efficient in the Southern Hemisphere, and the amplitude of the precipitation is larger in the southern tropics than in the northern tropics. This influence is offset by the impact of the Northern Hemisphere surface westerlies in the control case of the stripped-down model.

5.2. Fast Mechanism of Propagation: Advection of Vorticity

[59] In the presence of a mean meridional wind (Cases Ctrl′ and NoU_s), the oscillation is faster, in the intraseasonal range, and the precipitation anomalies clearly propagate northward throughout the tropics (Figure 6). This results from a fast mechanism that reinforces the slow mechanism described in the previous section, and creates a continuity in the pattern of precipitation anomalies. Here, we analyze this

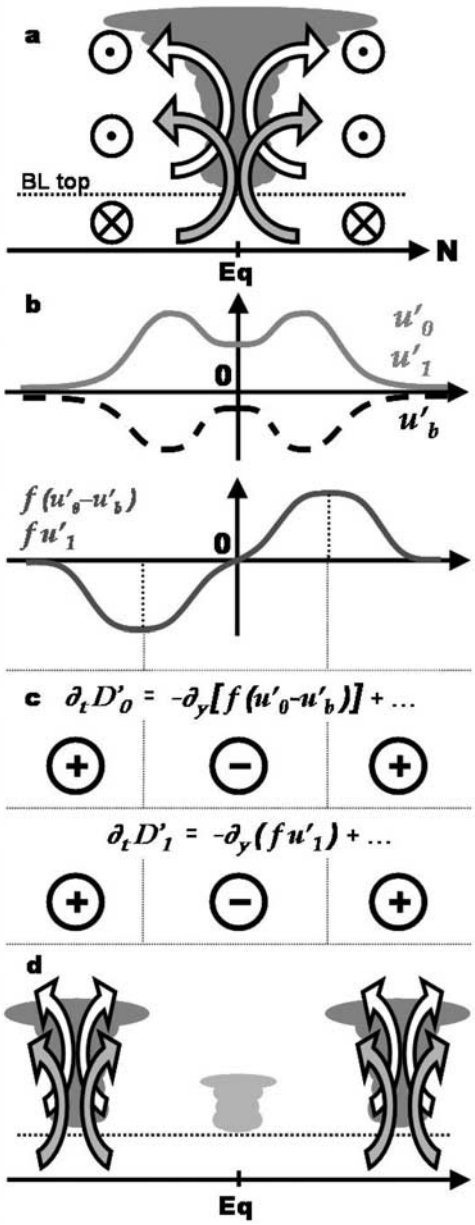

Figure 7. Mechanism of the oscillation in Case No$\mathcal{V}_1$ U_s: (a) convection at the equator creates a Hadley-like anomalous circulation that is (b) characterized by upper tropospheric westerlies and low-level easterlies. (c) Via Coriolis acceleration, these anomalous zonal wind create barotropic and baroclinic divergence away from the equator while destroying divergence at the equator. (d) This divergence pattern triggers convection away from the equator and damps equatorial convection.

fast mechanism in the control case of the stripped-down model.

[60] The model's oscillations feature the same dynamical structure as the nonlinear oscillations described in BS. A maximum of barotropic divergence leads the maximum of precipitation by about 3 degrees of latitude and this divergence maximum slightly lags a maximum of barotropic vorticity. The maximum in baroclinic divergence lags the maximum of precipitation, and is a response to the temperature forcing (not shown). This structure is very similar to the composites of observations and reanalysis [*Jiang et al.*, 2004; *Goswami*, 2005] and shows that the barotropic divergence is responsible for the northward propagation of precipitation anomalies.

[61] The maximum of barotropic vorticity generates the maximum in barotropic divergence by Coriolis acceleration, in a process similar to Ekman pumping, as can be seen from equation (34). Away from the equator, the gradient of Coriolis acceleration $-\partial_y[f(u'_0 - u'_b)]$ is dominated by $-f\partial_y u'_0 = f\zeta'_0$ (1) because surface friction keeps the ABL velocity and vorticity small and (2) because f varies on planetary scales while u'_0 varies on regional scales, so that the β term $-\beta u'_0$ is one order of magnitude smaller than $f\zeta'_0$. Therefore, if a maximum of ζ'_0 is located north of the convection maximum, the contribution of the Coriolis acceleration to the tendency of D'_0 creates a maximum of D'_0 north of the convection center.

[62] The existence of a maximum of ζ'_0 north of the maximum of precipitation is due to advection of baroclinic vorticity by the mean meridional baroclinic flow. Indeed, if we neglect the β term away from the equator, the equation for the anomalous barotropic vorticity ζ'_0 can be derived from equation (31) as follows:

$$\partial_t \zeta'_0 \approx -\langle V_1^2 \rangle \mathcal{V}_1 \partial_y \zeta'_1 - f D'_0 \tag{36}$$

where $\zeta'_1 = -\partial_y u'_1$ is the anomalous baroclinic vorticity. The term responsible for the vertical shear mechanism [*Jiang et al.*, 2004] is absent from (36), not because it is small in the control calculations with the full model (it is not) but because we have intentionally removed it from the stripped-down model by setting $\overline{u_1}$ to zero. The second term in equation (36) tends to create a minimum of barotropic vorticity colocated with the maximum of barotropic divergence and is therefore a damping term. The first term is the mean baroclinic advection of the anomalous baroclinic vorticity; it can account for the maximum of ζ'_0 north of the maximum of D'_0.

[63] Figure 8 illustrates the mechanism by which the entire structure, with its baroclinic and barotropic components, propagates northward. Consider an off-equatorial maximum of precipitation in the northern tropics, with the associated cyclonic circulation (Figure 8a). This circulation implies a maximum of the gradient of ζ'_1 north of the maximum of precipitation and minimum south of it (Figure 8b). Considering a southward baroclinic mean wind $\mathcal{V}_1 < 0$, the mean baroclinic advection of ζ'_1 creates (resp. destroys) barotropic vorticity north (resp. south) of the maximum of precipitation (Figure 8c). This results in a maximum of ζ'_0 north of the maximum of precipitation (Figure 8d) that in turn creates barotropic divergence and causes the northward propagation of the precipitation maximum. This mechanism clearly shows the predominant role of the mean baroclinic wind in the northward propagation.

[64] Since the rotation of the Earth is involved in both the establishment of a cyclonic circulation around the precipitation maximum and the contribution of the vorticity to the divergence tendency, the mechanism of propagation is the same in the Southern Hemisphere, except that a minimum

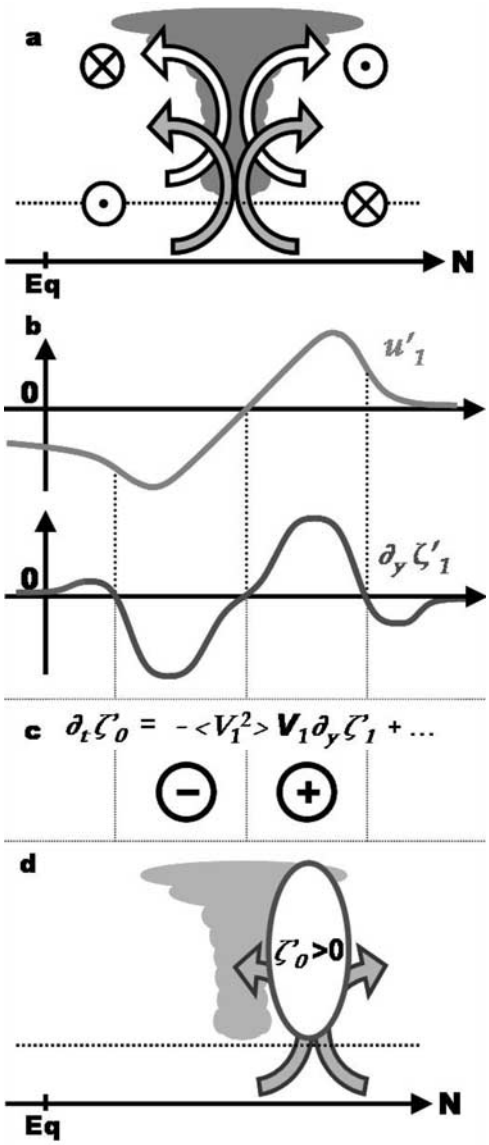

Figure 8. Mechanism of northward propagation: (a) convection in the northern tropics creates an anomalous cyclonic circulation characterized by baroclinic easterlies south of the convection center and baroclinic westerlies north of it. (b) This zonal wind pattern corresponds to a positive (negative) gradient of baroclinic vorticity north (south) of the convection. (c) Advection of baroclinic vorticity by the basic-state baroclinic wind creates barotropic vorticity north of the convection center (d) that in turn creates barotropic divergence via Coriolis acceleration and cause a northward shift of the convection.

of barotropic vorticity, rather than a maximum, is located north of the maximum of precipitation.

5.3. Fast Mechanism of Reinitiation: Advection of Zonal Momentum

[65] In the control case, an additional mechanism explains the fast reinitiation of convection at the equator when the propagating TCZ reaches 20–25°N. This reinitiation is due to equatorial ABL convergence as in the observations [*Wang et al.*, 2006]. At the equator, the Coriolis parameter is zero. The tendency of the barotropic divergence can thus be approximated by:

$$\partial_t D'_0 \approx -\tilde{\mu}\left[\beta\left(u'_0 - u'_b\right) + \langle a_1^+ \rangle \kappa \, \partial_y^2 T'_1\right] \tag{37}$$

As noted before, the last term of this equation tends to reinforce the current situation (divergence or convergence). Because u'_b is only driven by horizontal diffusion at the equator (see equation (33)), the term in u'_b is small and the time evolution of D'_0 is driven by the term in u'_0.

[66] At the equator, the tendency of the u'_0 can be approximated by the mean advection of anomalous zonal momentum:

$$\partial_t u'_0 \approx -\langle V_1^2 \rangle \mathcal{V}_1 \partial_y u'_1, \tag{38}$$

[67] Figure 9 shows how this advection is responsible for the reinitiation of convection at the equator. We now consider a maximum of precipitation around 20°N, with the associated cyclonic circulation (Figure 9a). This circulation implies a minimum of u'_1 in the northern tropics, south of the maximum of precipitation, and therefore a negative gradient of u'_1 south of this minimum. Considering that, in the control case, the amplitude of the oscillation is larger in the northern tropics than in the southern tropics, the region of negative gradient of u'_1 extends into the equatorial zone (Figure 9b). According to equation (38), with $\mathcal{V}_1 < 0$, the advection of u'_1 creates barotropic easterlies above the equator (Figure 9c) that in turn create barotropic divergence and convection in the equatorial zone (Figure 9d).

[68] Note that the fast mechanisms for both propagation and reinitiation are acting on the divergence D'_0 through the gradient of Coriolis acceleration as does the slow mechanism in Case No$\mathcal{V}_1$ U_s. The fast and slow mechanisms thus interact constructively.

5.4. Influence of the Wind-Induced Surface Fluxes

[69] In section 3, as well as in BS, the wind-induced surface fluxes appear crucial to the instability. On the other hand, the cases NoU_s and No$\mathcal{V}_1 U_s$ show that instability can be obtained without the surface flux feedback if model parameters are varied in the right way (e.g., decreasing τ_c). The wind-induced surface fluxes are therefore only one of the contributors to the instability, although an important one, and essential in our control case. Because the precipitation is proportional to the CAPE $\mathcal{E}'$, we can study the time evolution of $\mathcal{E}'$ to understand the role of the surface fluxes. Using equation (20), the tendency of $\mathcal{E}'$ can be written as the weighted sum of the budgets of humidity and energy of the ABL and free troposphere. This can be formulated as follows:

$$\partial_t \mathcal{E}' = Adv_{\mathcal{E}} + Conv_{\mathcal{E}} + SHF_{\mathcal{E}} + Rad_{\mathcal{E}} + Diff_{\mathcal{E}}, \tag{39}$$

where $Adv_{\mathcal{E}}$ is the resulting effect on $\mathcal{E}'$ of the advective tendencies of s_b, q_b, q_1, and T_1. $Conv_{\mathcal{E}}$, $Rad_{\mathcal{E}}$, $Diff_{\mathcal{E}}$, and $SHF_{\mathcal{E}}$ are, respectively, the contributions of convective, radiative, diffusive processes and surface fluxes on the time evolution of $\mathcal{E}'$. Advection and convection are the main contributions to the tendency of $\mathcal{E}'$. The convection acts to reduce $\mathcal{E}$: it

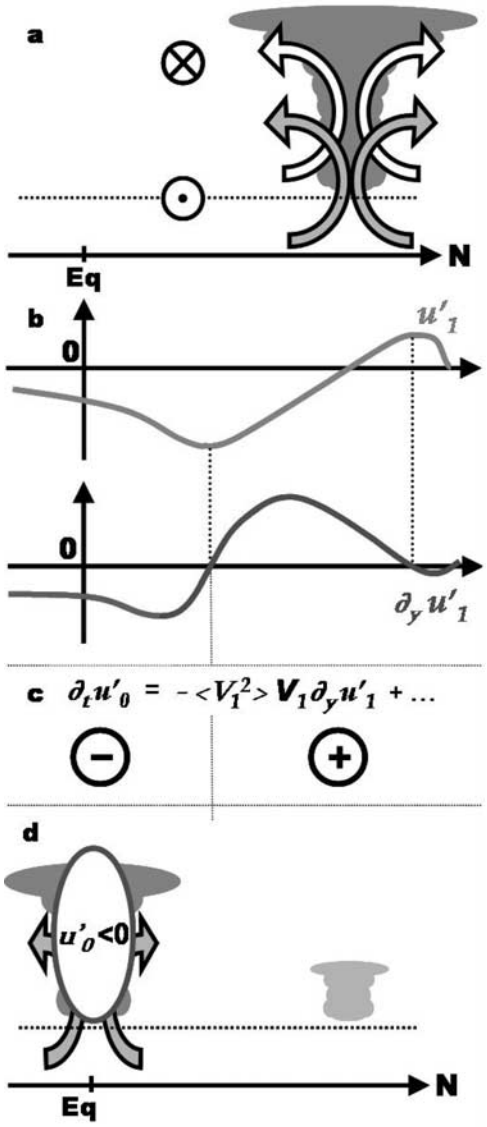

Figure 9. Mechanism of equatorial reinitiation: (a) convection away from the equator creates a cyclonic circulation characterized by baroclinic easterlies south of the convection. (b) When the center of convection is sufficiently far north, these easterlies have a maximum in the northern tropics, and (c) advection of baroclinic momentum by the basic-state baroclinic wind creates barotropic easterlies over the equator (d) that in turn create barotropic divergence via β Coriolis acceleration and reinitiate convection at the equator.

can be shown from equations (18)–(20) that $Conv_{\mathcal{E}} = -\epsilon_c \mathcal{E}'$. $Conv_{\mathcal{E}}$ is therefore anticorrelated with $\mathcal{E}'$ and convection reduces the instability of the base flow. In the previous sections, we showed that low-level convergence is instrumental in destabilizing the atmosphere to cause the propagation or reinitiation of convection: the advection $Adv_{\mathcal{E}}$ is therefore an important contributor to the instability of the base flow and the northward propagation. $SHF_{\mathcal{E}}$ is the third largest source of $\mathcal{E}'$; because $\mathcal{E}'$ depends on q'_b and s'_b only through their sum h'_b, the contribution of surface fluxes is proportional to the total surface heat flux:

$$SHF_{\mathcal{E}} = \mathcal{E}_b(E' + H'), \tag{40}$$

Figure 3b shows the oscillatory component of the total surface fluxes superimposed on the precipitation, which is equivalent to superimposing $SHF_{\mathcal{E}}$ on $\mathcal{E}'$. Surface flux maxima, driven by the wind perturbations, appear south of the precipitation maxima, with a large overlap between areas of positive P' and those of positive surface flux anomalies.

[70] Energetically, the instability of the mode requires that temperature and heating be positively correlated. In this mode, heating is dominated by the latent heat release by condensation, thus instability requires that temperature and precipitation be positively correlated. The temperature anomaly in the computed mode, as in observations of northward propagating monsoon rainbands (but unlike in convectively coupled gravity or Kelvin waves), slightly lags the precipitation anomaly. Since the surface flux anomalies also lag precipitation, they will tend, by drawing the precipitation anomalies toward lower latitude at a given time (or toward later time, at a fixed latitude), to increase the correlation between precipitation and temperature, thus enhancing the instability.

[71] As noted above, the surface flux maxima are located south of the precipitation maxima in Figure 3b. The surface fluxes are thus expected to oppose or to slow down the northward propagation. Indeed, the results of the stripped-down model show that the period of the unstable mode is shorter in Case NoU_s (without surface westerlies) than in the control case Ctrl′. If we consider an off-equatorial maximum of convection such as in Figure 8a, the cyclonic circulation around it creates anomalous surface westerlies (respectively easterlies) south (resp. north) of the convection. These anomalous winds interact constructively with the background westerlies south of the convection maximum to increase the surface fluxes there.

[72] The wind-induced surface fluxes also modulate the amplitude of precipitation. In Case No$\mathcal{V}_1$, this amplitude is larger in the northern tropics than near the equator and in the Southern Hemisphere, while the amplitudes are equal in Case No$\mathcal{V}_1 U_s$. The mechanism of this modulation is quite straightforward. If we consider a double ITCZ configuration in the presence of mean surface westerlies in the northern tropics, the surface fluxes are increased by the perturbation surface westerlies underneath and south of the northern TCZ. This reinforces the precipitation in the northern TCZ. Conversely, when there is a single equatorial ITCZ and the anomaly of precipitation is negative in the northern TCZ, the surface fluxes are decreased by the perturbation surface easterlies in the Northern Hemisphere. As a result, the amplitude of the oscillation is increased by the surface fluxes in the northern TCZ. On the other hand, mean trade winds, either in the northern or southern tropics, would reduce the amplitude of the TCZ oscillation there.

5.5. Vertical Shear of Zonal Versus Meridional Wind

[73] To evaluate whether the "vertical shear mechanism" can be an alternative mechanism for northward propagation

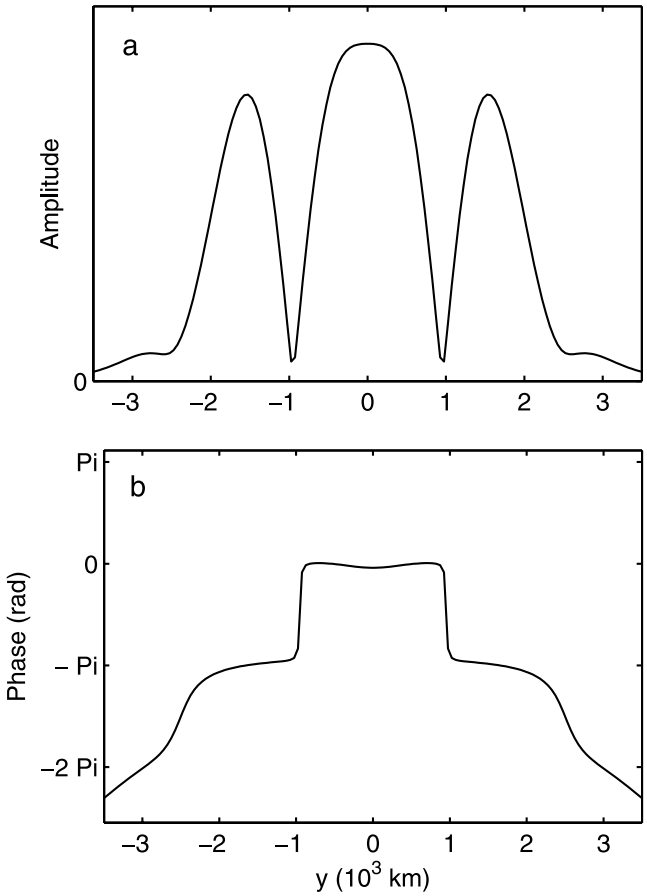

Figure 10. Precipitation amplitude and phase of the unstable mode for the stripped-down model in the configuration used by *Jiang et al.* [2004].

in our model, we perform a last experiment with our stripped-down model in the configuration used by *Jiang et al.*'s [2004] theoretical analysis. In this configuration, there is no gradient of humidity nor temperature and no mean flow except for a constant zonal baroclinic flow, that we set to $\overline{u}_1 = -16$ ms^{-1}. We also use the modified parameters (τ_c = 0.15 d, τ_R = 30 d). This experiment is identical to Case NoU_s, except that the meridional baroclinic basic flow is replaced by a zonal baroclinic basic flow. In this configuration, our model does have a linearly unstable mode with a period of 67.2 d and an *e*-folding time of 90.8 d. The structure of this mode is displayed in Figure 10; it is very similar to that of the no-mean-flow unstable mode. Again, $\overline{u}_1$ appears as a contributor to instability. Moreover, $\overline{u}_1$ appears to halve the period of the oscillation between single and double ITCZ that is present in the no-mean-flow case, and this shows that the "vertical shear mechanism" can contribute to the slow mechanism of oscillation. But it does not produce a northward propagation by itself in our model, while the meridional baroclinic basic flow does cause northward propagation in Case NoU_s. In our model, the anomalous vertical advection of the mean zonal shear appears to complement other processes and to accelerate the resulting oscillation or propagation rather than to be the principal cause of oscillations as postulated in the "vertical shear mechanism."

6. Summary and Discussion

[74] We used the linear QTCM2 in an aquaplanet, axisymmetric, β-plane configuration to study the properties of the simulated intraseasonal oscillation. We studied the sensitivity of the unstable mode to the different components of the basic state in order to understand the key elements responsible for the northward propagation. Our main results are:

[75] 1. The instability of the seasonal monsoon flow is controlled by a combination of factors. The leading ones are the wind-induced surface heat fluxes and the mean meridional flow $\overline{v}_1$. Both these effects depend on the base state flow. The baroclinic mean zonal wind $\overline{u}_1$ also has a strong destabilizing effect, and the advective contribution of the ABL flow $\overline{\mathbf{v}}_b$ has a moderate destabilizing effect. By suppressing the oscillation in the Southern Hemisphere, the mean thermodynamic gradients of temperature and humidity have a strong stabilizing impact.

[76] 2. The frequency of the unstable mode is controlled by the mean meridional flow $\overline{v}_1$, and increases with $|\overline{v}_1|$. The direction of propagation is also controlled by the mean meridional baroclinic wind $\overline{v}_1$. The existence of mean monsoonal upper tropospheric northerlies and lower tropospheric southerlies in the tropics ($\overline{v}_1 < 0$) causes northward propagation. This occurs via the mean baroclinic advection in the budget of zonal barotropic momentum. This advection controls the mechanisms of both propagation and reinitiation. By slowing down the northward propagation via wind-induced surface fluxes, the surface mean westerlies modulate the period. Mechanisms associated with the baroclinic mean zonal wind $\overline{u}_1$, such as the "vertical shear mechanism" [*Jiang et al.*, 2004], accelerate the northward propagation.

[77] 3. The latitudinal modulation of amplitude results from the alteration by the mean flow of a three-maximum structure intrinsic to the system regardless of the mean flow. This no-mean-flow structure seems to primarily set the spatial scale of the propagation with a precipitation maximum at about one equatorial radius of deformation from the equator. Negative $\overline{v}_1$ tends to favor the oscillation in the Southern Hemisphere while the surface mean westerlies tend to enhance it in the Northern Hemisphere. The latter effect is dominant, but the main factor that confines the oscillation to the northern tropics is that the mean thermodynamic environment is unfavorable for convection in the Southern Hemisphere.

[78] These properties result from the mechanisms of northward propagation and reinitiation at the equator. The mean meridional flow $\overline{v}_1$ intervenes in both mechanisms. The propagation mechanism explains the creation of a maximum of barotropic vorticity north of the convection center by mean baroclinic advection of the baroclinic vorticity ζ_1' associated with the cyclonic circulation around the convection center. This barotropic vorticity in turn creates the barotropic divergence (i.e., ABL convergence) that leads convection. The equatorial reinitiation mechanism explains the resurgence of convection over the equator by the creation of barotropic divergence via the β effect

associated with barotropic easterlies u'_0. This negative u'_0 results from the mean baroclinic advection of baroclinic momentum u'_1 that in turn results from the cyclonic circulation due to the convection maximum around 20°N.

[79] The propagation mechanism found here differs from that proposed in previous studies [*Jiang et al.*, 2004; *Drbohlav and Wang*, 2005; *Wang et al.*, 2006]. In these studies, the "vertical shear mechanism" proposed to explain the vorticity pattern relies on the gradient of vertical advection of the mean easterly vertical shear $\overline{u}_1$. This term is of the same order of magnitude as the mean advection of anomalous baroclinic vorticity in the barotropic vorticity budget of the full nonlinear model used in BS (not shown). $\overline{u}_1$ also has a strong impact on the stability of the base flow and modulates the period by about 20%. Thus, the vertical shear mechanism is active in our model, although it does not appear to be the dominant mechanism because (1) most of the properties of the oscillation are conserved when $\overline{u}_1$ is set to zero as in experiment Nou_1 (see section 3) and (2) $\overline{u}_1$ alone does not cause northward propagation in the stripped-down model (see section 5.5).

[80] Diverse aspects of the 30- to 60-d mode have not been investigated here. Future work will investigate the role of the coupling with the oceanic (and continental) surface that have been shown to modulate the propagation [*Sengupta et al.*, 2001; *Fu and Wang*, 2004]. Investigating the longitude-dependent effects that have a significant impact on the reinitiation and development of the northward propagating TCZ [*Jiang and Li*, 2005; *Wang et al.*, 2006] or on the tropics-extratropics interaction [*Lin et al.*, 2000] are ongoing challenges, although it is beyond the reach of our current framework.

Appendix A: Sensitivity to the Main Parameters

A1. Sensitivity to the Convective and Radiative Timescales

[81] The convective and radiative timescales control the response of the thermodynamic variables to adiabatic processes. They are therefore expected to have an important impact on the behavior of the model. We use the results of this sensitivity study to modify the parameters of the model in section 4.

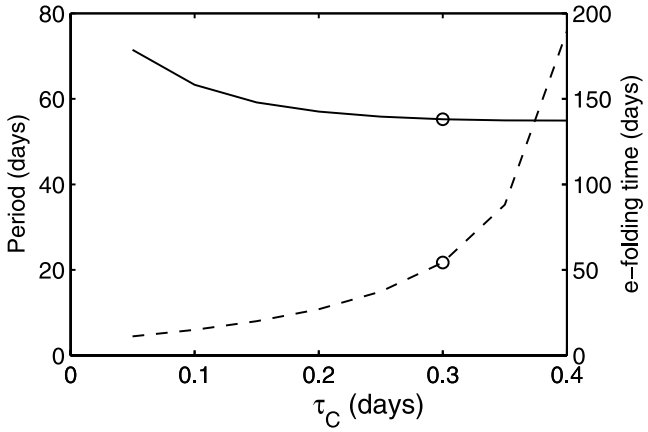

Figure A1. Sensitivity of the period (solid) and *e*-folding time (dashed) to the convective timescale τ_c. The circle indicates the control case.

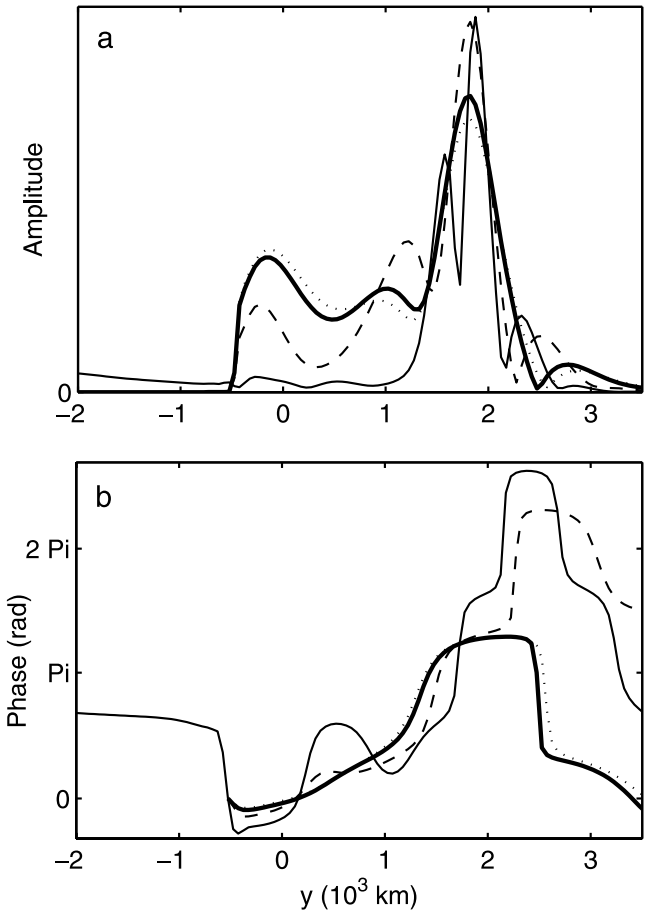

Figure A2. Precipitation amplitude and phase of the unstable mode in the control case (thick line), for τ_c = 0.4 d (dotted), for τ_c = 0.1 d (dashed) and one of the unstable modes for K = 0.15 (solid).

[82] Figure A1 shows that the *e*-folding time (i.e., the inverse of the growth rate) of the unstable mode increases with the convective timescale τ_c, and the base state becomes stable for $\tau_c > 0.4$ d. This sensitivity is common to models of the QTCM family and others using Betts-Miller closures, for which decreasing τ_c increases the instability in a variety of contexts [*Emanuel*, 1993; *Sobel and Gildor*, 2003; *Sobel et al.*, 2004]. The period of the mode decreases with τ_c, but it stays in a limited range of intraseasonal values between 55 and 75 d (Figure A1).

[83] Figure A2 shows the amplitude and phase of the unstable mode for τ_c = 0.1, 0.3 and 0.4 d. The structure of the mode changes little when τ_c is increased from the control value (see dotted line in Figure A2). On the other hand, this structure is significantly modified when τ_c is decreased: the equatorial maximum of precipitation amplitude is damped, the third maximum around 10°N amplifies, and the monsoonal maximum of amplitude is more concentrated (Figure A2a). For small τ_c, the propagation also seems to be concentrated around the monsoonal maximum

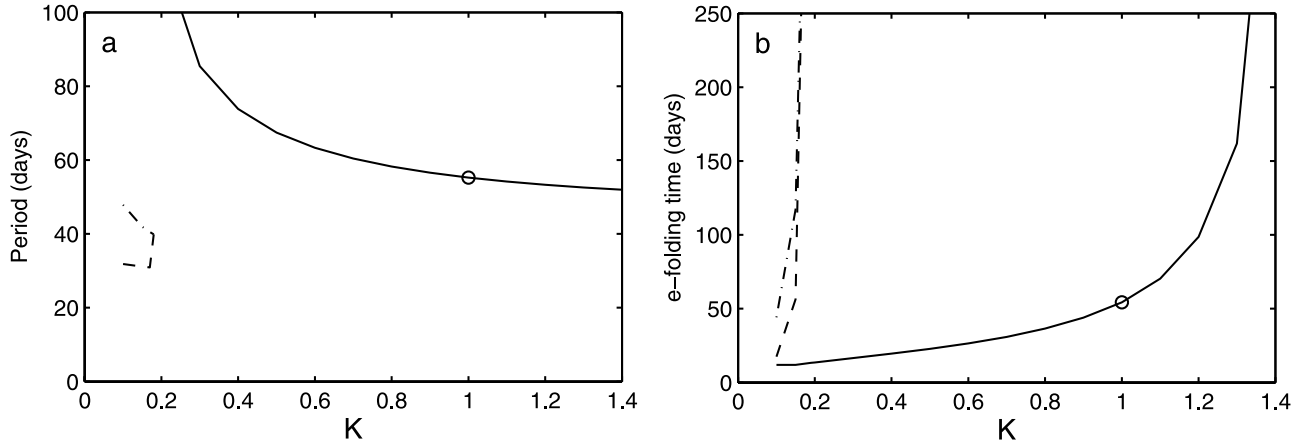

Figure A3. Sensitivity of the (a) period and (b) *e*-folding time to the intensity of the diffusion *K*. The dashed and dash-dotted lines show the additional modes that appear for low diffusion. The circle indicates the control case.

of precipitation amplitude: the phase changes slowly from the equator to 15°N, and faster north of this latitude. Also, the phase reversal that characterizes the northward extremity of the TCZ's propagation occurs further south at low τ_c than in the control case (Figure A2b).

[84] The unstable mode is not very sensitive to changes in the radiative timescale τ_R. The period of the mode exhibits almost no sensitivity to τ_R. The *e*-folding time is slightly more sensitive than the period and it decreases with τ_R. Within the range of interest, the structure of the mode is very similar to that of the control case; the small differences follow the same relationship between structure and *e*-folding time as in the case of changes in the convective timescale τ_c (not shown).

A2. Sensitivity to the Surface Friction and Diffusion

[85] Earlier work leads us to suspect that the parameters controlling the surface friction and the diffusion will influence the scale selection of the unstable mode [*Jiang et al.*, 2004; *Bellon and Srinivasan*, 2006].

[86] We first study the sensitivity of the mode to the diffusion. To do so, we multiply both diffusion parameters k_v and k_q by a factor K that is varied systematically. Figure A3 shows the sensitivity of the period and *e*-folding time to K. The sensitivity to K is similar to the sensitivity to τ_c. The period decreases with K, but the dependence is weak near $K = 1$. The *e*-folding time increases with K, consistent with the dissipative nature of the diffusive terms. Decreasing the diffusion favors intense, localized, self-enhancing disturbances that tend to propagate slowly. The structure of the mode follows the same relationship with the *e*-folding time as the one described for the sensitivity to τ_c: for small K, the equatorial maximum of precipitation amplitude is smaller, and a double, concentrated maximum appears between 10 and 20°N. Figure A2 shows an extreme case for $K = 0.15$, where the equatorial maximum almost disappears and the northward propagation is concentrated over two localized maxima between 10 and 20°N. When decreasing K below 0.2, one and then two additional intraseasonal modes appear, with similar structure to the first one and periods in the 30- to 50-d range. For $K < 0.1$, some synoptic unstable modes also appear. These latter may or may not have any relevance to the real atmosphere. We do not discuss them further here, as our interest is in intraseasonal timescales.

[87] Figure A4 shows the sensitivity of the period and *e*-folding time to the surface friction timescale ϵ_b^{-1}. The base state is most unstable for ϵ_b^{-1} of about 1 d. Some insight into this can be gained by considering the ABL momentum budgets. At first order, the budget of zonal momentum in the ABL expresses a quasi-balance between the friction and the Coriolis force. The zonal wind can thus be approximated by $u_b \approx fv_b/\epsilon_b$. In the meridional momentum budget, the Coriolis acceleration can thus be approximated by an off-equatorial damping term $-f^2 v_b/\epsilon_b$ that increases with ϵ_b^{-1}. This damping and the surface friction $-\epsilon_b v_b$ are the two terms that depend on ϵ_b in the meridional momentum budget. For large ϵ_b, the surface friction opposes any boundary layer flow, and therefore stabilizes the flow. For small ϵ_b, the Coriolis term limits the instability of the base flow. If we consider the ABL flow to be in quasi-equilibrium

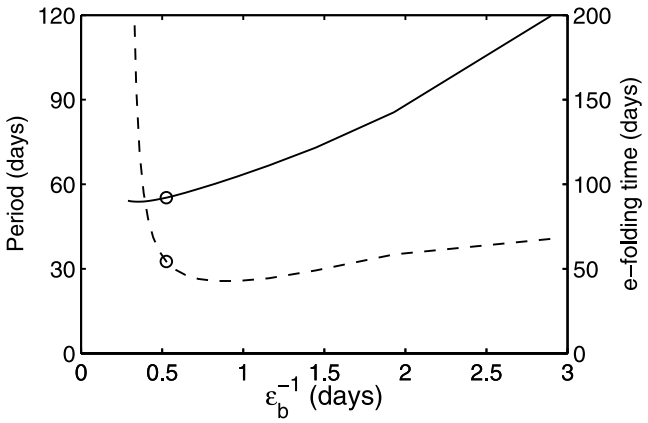

Figure A4. Sensitivity of the period (solid) and *e*-folding time (dashed) to the surface friction timescale $\in_b{}^{-1}$. The circle indicates the control case.

with the pressure forcing, the approximate meridional momentum equation is:

$$\left(\epsilon_b + \frac{f^2}{\epsilon_b}\right) v_b = -\partial_y \phi_s. \tag{A1}$$

Given $\partial_y \phi_s$, the largest v_b occurs for $\epsilon_b \sim |f|$, i.e., of the order of 1 d at low latitude.

[88] The period increases significantly with increasing ϵ_b. This is due to the increase of u_b with ϵ_b^{-1} that enhances the wind-induced surface heat fluxes. We further comment in section 5 how this wind-induced effect can both destabilize and slow down the propagation. The structure of the mode is insensitive to changes in ϵ_b (not shown).

[89] **Acknowledgments.** We thank J. Srinivasan for useful comments. This work was supported by a fellowship from the David and Lucile Packard Foundation and NSF grant ATM-05-42736.

References

Bellon, G., and A. H. Sobel (2008), Poleward-propagating intraseasonal monsoon disturbances in an intermediate-complexity axisymmetric model, *J. Atmos. Sci.*, *65*, 470–489.

Bellon, G., and J. Srinivasan (2006), Comment on "Structures and mechanisms of the northward propagating boreal summer intraseasonal oscillation", *J. Clim.*, *19*, 4738–4743.

Betts, A. K. (1986), A new convective adjustment scheme. Part I: Observational and theoretical basis, *Q. J. R. Meteorol. Soc.*, *112*, 677–691.

Betts, A. K., and M. J. Miller (1986), A new convective adjustment scheme. Part II: Single column tests using GATE wave, BOMEX, ATEX and arctic air-mass data sets, *Q. J. R. Meteorol. Soc.*, *112*, 693–709.

Chatterjee, P., and B. N. Goswami (2004), Structure, genesis and scale selection of the tropical quasi-biweekly mode, *Q. J. R. Meteorol. Soc.*, *130*, 1171–1194.

Drbohlav, H.-K., and B. Wang (2005), Mechanism of the northward-propagating intraseasonal oscillation: Insights from a zonally symmetric model, *J. Clim.*, *18*, 952–972.

Emanuel, K. A. (1987), An air-sea interaction model of intraseasonal oscillations in the tropics, *J. Atmos. Sci.*, *44*, 2324–2340.

Emanuel, K. A. (1993), The effect of convective response time on wishe modes, *J. Atmos. Sci.*, *50*, 1763–1775.

Fu, X., and B. Wang (2004), Differences of boreal-summer intraseasonal oscillations simulated in an atmosphere-ocean coupled model and an atmosphere-only model, *J. Clim.*, *17*, 1263–1271.

Gadgil, S., and J. Srinivasan (1990), Low frequency variation of tropical convergence zone, *Meteorol. Atmos. Phys.*, *44*, 119–132.

Gadgil, S., P. V. Joseph, and N. V. Joshi (1984), Ocean-atmosphere coupling over monsoon regions, *Nature*, *312*, 141–143.

Goswami, B. N. (2005), South Asian monsoon, in *Intraseasonal Variability in the Atmosphere-Ocean Climate System*, edited by W. K. M. Lau and D. E. Waliser, pp. 19–61, Springer, Berlin.

Goswami, B. N., and R. S. Ajaya Mohan (2001), Intraseasonal oscillations and interannual variability of the Indian summer monsoon, *J. Clim.*, *14*, 1180–1198.

Goswami, B. N., and J. Shukla (1984), Quasi-periodic oscillations in a symmetric general circulation model, *J. Atmos. Sci.*, *41*, 20–37.

Graham, N. E., and T. P. Barnett (1987), Sea surface temperature, surface wind divergence and convection over tropical oceans, *Science*, *238*, 657–659.

Jiang, X., and T. Li (2005), Reinitiation of the boreal summer intraseasonal oscillation in the tropical Indian Ocean, *J. Clim.*, *18*, 3777–3795.

Jiang, X., T. Li, and B. Wang (2004), Structures and mechanisms of the northward propagating boreal summer intraseasonal oscillation, *J. Clim.*, *17*, 1022–1039.

Kemball-Cook, S., and B. Wang (2001), Equatorial waves and air-sea interaction in the boreal summer intraseasonal oscillation, *J. Clim.*, *14*, 2923–2942.

Lawrence, D. M., and P. Webster (2002), The boreal summer intraseasonal oscillation: Relationship between northward and eastward movement of convection, *J. Atmos. Sci.*, *59*, 1593–1606.

Lin, J. W. B., J. D. Neelin, and N. Zeng (2000), Maintenance of tropical intraseasonal variability: Impact of evaporation-wind feedback and midlatitude storms, *J. Atmos. Sci.*, *57*, 2793–2823.

Nanjundiah, R., J. Srinivasan, S. Gadgil, and P. Webster (1992), Intraseasonal variation of the Indian summer monsoon. Part II: Theoretical aspects, *J. Meteorol. Soc. Jpn.*, *70*, 529–550.

Neelin, J. D., and N. Zeng (2000), A quasi-equilibrium tropical circulation model—Formulation, *J. Atmos. Sci.*, *57*, 1741–1766.

Neelin, J. D., I. M. Held, and K. H. Cook (1987), Evaporation-wind feedback and low frequency variability in the tropical atmosphere, *J. Atmos. Sci.*, *44*, 2341–2348.

Sengupta, D., B. N. Goswami, and R. Senan (2001), Coherent intraseasonal oscillations of ocean and atmosphere during the Asian summer monsoon, *Geophys. Res. Lett.*, *28*, 4127–4130.

Sikka, D. R., and S. Gadgil (1980), On the maximum cloud zone and the ITCZ over Indian longitude during southwest monsoon, *Mon. Weather Rev.*, *108*, 1840–1853.

Sobel, A. H., and H. Gildor (2003), A simple time-dependent model of SST hot spots, *J. Clim.*, *16*, 3978–3992.

Sobel, A. H., and J. D. Neelin (2006), The boundary layer contribution to intertropical convergence zones in the quasi-equilibrium tropical circulation model framework, *Theor. Comput. Fluid Dyn.*, *20*, 323–350.

Sobel, A. H., C. S. Bretherton, H. Gildor, and M. E. Peters (2004), Convection, cloud-radiative feedbacks and thermodynamic ocean coupling in simple models of the Walker Circulation, in *Earth's Climate: The Ocean-Atmosphere Interaction*, *Geophys. Monogr. Ser.*, vol. 147, edited by C. Wang, S.-P. Xie, and J. A. Carton, pp. 393–405, AGU, Washington, D. C.

Wang, B., and X. Xie (1997), A model for the boreal summer intraseasonal oscillation, *J. Atmos. Sci.*, *54*, 71–86.

Wang, B., P. J. Webster, K. Kikuchi, T. Yasunari, and Y. Qi (2006), Boreal summer quasi-monthly oscillation in the global tropics, *Clim. Dyn.*, *27*, 661–675.

Zeng, N., J. D. Neelin, and C. Chou (2000), A quasi-equilibrium tropical circulation model—Implementation and simulation, *J. Atmos. Sci.*, *57*, 1767–1796.

G. Bellon, IRI, Columbia University, Lamont Campus, 61 Route 9W, Monell Building, Palisades, NY 10964-8000, USA. (gilles@iri.columbia.edu)

A. H. Sobel, Department of Applied Physics and Applied Mathematics, Columbia University, New York, NY 10027, USA.